JOURNAL OF SPACECRAFT AND ROCKETS
Vol. 46, No. 6, November–December 2009

Linear Covariance Analysis for Powered Lunar Descent and Landing

David K. Geller* and Daniel P. Christensen†
Utah State University, Logan, Utah 84322

DOI: 10.2514/1.38641

A baseline sensor suite consisting of a star camera, an altimeter, gyros, accelerometers, and a velocimeter is examined for the powered lunar descent landing problem using linear covariance techniques. The inertial navigation error during lunar powered descent and landing is determined, and the sensitivities to initial navigation errors, gravity model errors, and individual instrument errors are evaluated. Terrain-relative navigation sensors are introduced into the analysis, and a novel application of linear covariance analysis is used to iteratively determine the sensor specifications needed to meet a 100 m 3-σ landing-error requirement. The sensitivities of landing navigation error to sensor errors, environment modeling errors, and terrain map errors are determined.

Nomenclature

$\boldsymbol{a}$	=	acceleration, m/s^2
$\boldsymbol{b}$	=	vector bias
$\mathrm{Diag}(\boldsymbol{v})$	=	diagonal matrix with elements of vector **v** along the diagonal
d	=	correlation distance, m
$\hat{F}_{\hat{x}}$	=	Jacobian of the dynamics
$\boldsymbol{f}$	=	vector scale factor
$\hat{H}_{\hat{x}}(t_m)$	=	Jacobian of the measurement function at time t_m
h	=	altitude, m
$\boldsymbol{h}(\boldsymbol{x}, t)$	=	measurement function relating the state $\boldsymbol{x}$ to the measurement $\boldsymbol{z}$
$I_{n\times n}$	=	identity matrix
$\hat{K}(t_m)$	=	Kalman filter gain at time t_m
$\hat{K}_r$	=	controller position gain, s^{-2}
$\hat{K}_v$	=	controller velocity gain, s^{-1}
$\hat{K}_\omega$	=	controller attitude-rate gain, N · m · s/rad
$\hat{K}_\theta$	=	controller attitude gain, N · m/rad
$O_{m\times n}$	=	matrix of zeros
$\hat{P}(t_m^-)$	=	onboard filter covariance at time t_m just before measurement update
$\hat{P}(t_m^+)$	=	onboard filter covariance at time t_m just after measurement update
$\boldsymbol{p}$	=	parameters states
$\boldsymbol{q}$	=	quaternion indicated by boldface q
$\boldsymbol{q}_a^b$	=	quaternion representing the orientation of the b frame with respect to the a frame
R	=	covariance of discrete white noise process
$\boldsymbol{r}$	=	position of the lander, m
$\boldsymbol{r}_o$	=	position of the landing objective, m
S	=	strength of continuous vector white noise process
$\boldsymbol{T}$	=	torque, N · m
$\mathcal{T}_a^b$	=	direction cosine matrix representing the orientation of the b frame with respect to the a frame
$\boldsymbol{v}$	=	velocity of lander, m/s
$\mathbf{v}$	=	vector
$\mathbf{v}^a$	=	vector represented in coordinate frame a
$\boldsymbol{w}$	=	continuous white Gaussian process noise
$\mathbf{x}$	=	state vector
$\boldsymbol{z}$	=	sensor measurements
$\delta\boldsymbol{q}(\boldsymbol{\epsilon})$	=	quaternion associated with a small rotation, $\delta\boldsymbol{q}(\boldsymbol{\epsilon}) \approx \begin{pmatrix} \boldsymbol{\epsilon}/2 \\ 1 \end{pmatrix}$
$\delta\mathcal{T}(\boldsymbol{\epsilon})$	=	direction cosine matrix associated with a small rotation, $[\delta\mathcal{T}(\boldsymbol{\epsilon})] \approx I_{3\times3} - [\boldsymbol{\epsilon}\times]$
$\delta(t - t')$	=	Dirac delta function
$\delta_{mm'}$	=	Kronecker delta function
$\delta\boldsymbol{\theta}$	=	small-angle rotation vector, rad
$\boldsymbol{\varepsilon}$	=	environment states
$\boldsymbol{\epsilon}$	=	vector small-angle misalignment, rad
$\boldsymbol{\epsilon}$	=	small rotation vector
$[\boldsymbol{\epsilon}\times]$	=	cross product matrix defined by the ordinary cross product $[\boldsymbol{\epsilon}\times]\boldsymbol{v} = \boldsymbol{\epsilon} \times \boldsymbol{v}$
$\boldsymbol{\eta}$	=	continuous white Gaussian measurement noise
$\boldsymbol{\theta}$	=	large-angle rotation vector, rad
$\boldsymbol{\nu}$	=	discrete white Gaussian measurement noise
σ^2	=	steady-state variance of first-order Markov process
τ	=	correlation time constant, s
$\boldsymbol{\omega}$	=	inertial angular velocity of the lander, rad/s
$\otimes$	=	quaternion multiplication operator such that $\boldsymbol{q}_a^c = \boldsymbol{q}_b^c \otimes \boldsymbol{q}_a^b$ corresponds to the sequence of rotations $\mathcal{T}_a^c = \mathcal{T}_b^c \mathcal{T}_a^b$
$\hat{}$	=	parameters, variables, and functions associated with the flight algorithms
$\tilde{}$	=	measured values
$\bar{}$	=	reference or nominal values

Subscripts

accel	=	acceleration sensor
act	=	actuators
com	=	flight command
comp	=	corrected or compensated
grav	=	gravity model
gyro	=	inertial angular velocity sensor
l	=	lander
map	=	terrain map
moon	=	lunar parameters
o	=	landing objective
s	=	sensors
starcam	=	star camera
terrain	=	lunar terrain
thrust	=	thrust actuators
torque	=	torque actuators
trnpos	=	terrain-relative position sensor
trnang	=	terrain-relative angular sensor
vel	=	surface-relative velocity sensor

Received 19 May 2008; revision received 14 August 2009; accepted for publication 16 August 2009.

*Assistant Professor, Mechanical and Aerospace Engineering Department. Senior Member AIAA.

†Graduate Student, Mechanical and Aerospace Engineering Department.

a = translational acceleration
α = angular acceleration
Δr = change in position

Superscripts

i = inertial frame
l = lander body frame
s = lunar surface frame
starcam = star-camera frame
trn = terrain-relative navigation sensor frame
vel = velocimeter frame

I. Introduction

A GENERAL linear covariance (LinCov) analysis [1] is a statistical analysis tool that produces Monte Carlo-like results in a fraction of the time. Because of its speed, it is often the tool of choice when there are many options and trades to be considered in the early design phases of a guidance, navigation, and control (GNC) system. Although LinCov may not offer the detailed high-fidelity analysis of a complex Monte Carlo simulation, it is usually accurate enough for early design analysis. In the case of traditional GNC space systems, the differences between LinCov and Monte Carlo results are typically less than 10% [2], though results need to be periodically verified.

The purpose of this research is to apply LinCov to the problem of powered lunar descent and landing navigation and to determine the sensitivity of navigation performance to sensor selection and accuracy. Although both LinCov and Monte Carlo techniques have previously been applied to this problem [3–5], this research is new in that it first evaluates the navigation performance for an inertial navigation system with and without terrain-relative navigation (TRN) and then introduces a novel application of LinCov analysis to iteratively determine the TRN sensor specifications needed to meet a 100 m 3-σ relative navigation landing-error requirement. Because the total landing error is often dominated by navigation error, this paper focuses on landing navigation performance. First, a navigation system instrumented with gyros, accelerometers, a star camera, a velocimeter, and an altimeter is considered and then later a TRN sensor is added to the sensor suite. The total position control error or landing *dispersion* will be the focus of a future study.

As with a Monte Carlo simulation, there is a need to validate the models in a LinCov simulation and assess their accuracy. No simulation, including Monte Carlo simulations, is 100% accurate. The LinCov simulation in this paper has been validated by comparing the results with Apollo data, by making comparisons with Monte Carlo simulations, and by using good engineering judgment. Deorbit position and velocity errors consistent with Apollo data [6] were used to initialize the LinCov simulation, and the resulting navigation errors at landing were found to be approximately the same as published in Apollo-era literature [6]. Additionally, many of the models in this LinCov simulation have been validated directly by Monte Carlo analysis [1,2,7]. This includes all the rotational and translational dynamics models, attitude determination and control algorithm models, and sensor models including star cameras, gyros, accelerometers, and optical cameras. The only models not previously validated are the relatively simple models for the altimeter, velocimeter, and the terrain navigation sensor. The models for these sensors are, however, similar to models used in other lunar descent navigation simulation tools [4,5]. Finally, as with any linear covariance simulation it is always important to apply good engineering judgment in deciding whether or not the results of a linearized system are going to be meaningful. In the case of lunar powered descent, they are. This is evidenced by the fact that the lunar-landing problem can be characterized by Kalman filters for navigation and gain scheduling (polynomial curve fits) for guidance. Gain scheduling and Kalman filters only work well when the a linearized model of the system is appropriate.

The math models for the true environment and GNC flight algorithms are presented in Secs. II and III. Then the baseline sensor errors, environment errors, and nominal descent trajectories are presented in Sec. IV. Inertial navigation performance results are presented in Sec. V, and the sensitivity to inertial sensor accuracy and environment modeling uncertainties is discussed. TRN sensors are introduced into the analysis in Sec. VI, and the TRN sensor specifications needed to meet a 100 m 3-σ relative navigation landing-error requirement are determined. Finally, the sensitivity of relative navigation performance to sensor errors, environment modeling uncertainties, and terrain map errors are presented and discussed.

II. Truth Models

The LinCov analysis conducted in this paper is based upon the conceptual Monte Carlo simulation shown in Fig. 1. The simulation consists of *truth* models for sensors, actuators, and the environment and flight software models for navigation (e.g., the onboard Kalman filter), translational and rotational control, and pointing algorithms. The LinCov analysis tool is based on linearized versions of the truth models and flight software models, which are in turn used to develop covariance propagation and update equations. The covariance equations are used to generate statistics on navigation error, trajectory position and velocity error, and attitude error. The attitude and trajectory errors are often referred to as *dispersions*.

The sensors onboard the lander include accelerometers, gyros, and a star camera for inertial navigation and an altimeter, a velocimeter, and either an angle- or position-based landmark recognition capability for surface-relative navigation. The combined hardware and software needed for landmark recognition is referred to as the *terrain-relative navigation* (TRN) sensor. The angle-based TRN provides line-of-sight angle information on the position of the lander relative to known landmarks. The position-based TRN provides a complete position vector from the landmark to the lander. The actuators onboard the lander consist of a set of thrusters to produce the desired thrust and torque.

The LinCov tool used in this analysis has $n = 84$ states. The states are divided into five major groups: landing objective, lunar lander, sensor parameter, actuator parameter, and environment:

$$\boldsymbol{x} = (\boldsymbol{x}_o, \boldsymbol{x}_\ell, \boldsymbol{p}_s, \boldsymbol{p}_{\text{act}}, \boldsymbol{\varepsilon})^T \tag{1}$$

The state of the landing objective is the position of the landing site in inertial coordinates:

$$\boldsymbol{x}_o = (\boldsymbol{r}_o^i)^T \tag{2}$$

The state of the lunar lander consists of the inertial position, inertial velocity, inertial to lander frame quaternion, and the inertial angular velocity of the lander in body coordinates:

$$\boldsymbol{x}_\ell = (\boldsymbol{r}^i, \boldsymbol{v}^i, \boldsymbol{q}_i^\ell, \boldsymbol{\omega}^\ell)^T \tag{3}$$

There are $n_p = 63$ sensor and actuator states in total. The actuator parameters $\boldsymbol{p}_a$ characterize the errors in the thrust forces and thrust torques:

$$\boldsymbol{p}_{\text{act}} = (\boldsymbol{p}_{\text{thrust}}, \boldsymbol{p}_{\text{torque}})^T \tag{4}$$

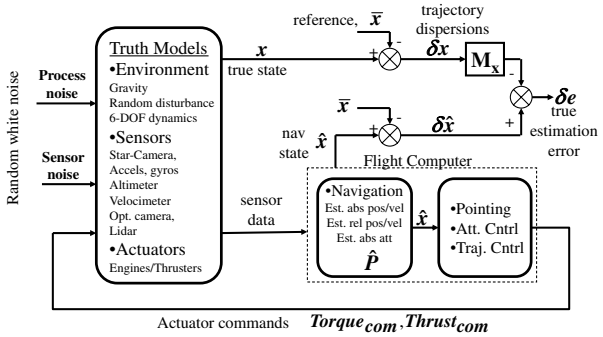

Fig. 1 Conceptual Monte Carlo simulation for GNC analysis.

It should be noted that because the control forces and torques are produced with a common set of thrusters, the thrust force and torque errors may be correlated. However, in this analysis they will be modeled as uncorrelated errors. The sensor parameters $\boldsymbol{p}_s$ characterize the errors for the accelerometers, gyros, velocimeter, TRN position sensor, TRN angle sensor, star camera, and altimeter:

$$\boldsymbol{p}_s = (\boldsymbol{p}_{\text{accel}}, \boldsymbol{p}_{\text{gyro}}, \boldsymbol{p}_{\text{vel}}, \boldsymbol{p}_{\text{trnpos}}, \boldsymbol{p}_{\text{trnang}}, \boldsymbol{p}_{\text{starcam}}, \boldsymbol{p}_{\text{alt}})^T \tag{5}$$

The sensor and actuator parameters consist of bias errors $\boldsymbol{b}$, scale-factor errors $\boldsymbol{f}$, and misalignment errors $\boldsymbol{\epsilon}$, all of which are modeled as first-order Markov processes. The elements of both sets are outlined in Table 1.

Finally, the $n_\varepsilon = 6$ environment states represent limited knowledge of the lunar environment. They consist of an error in the lunar gravity model $\boldsymbol{\varepsilon}^i_{\text{grav}}$ and an error in the onboard terrain map $\boldsymbol{\varepsilon}^s_{\text{map}}$ used by the TRN. Both are modeled as first-order Markov processes correlated by distance instead of time:

$$\boldsymbol{\varepsilon} = (\boldsymbol{\varepsilon}^s_{\text{map}}, \boldsymbol{\varepsilon}^i_{\text{grav}})^T \tag{6}$$

A. Dynamics and Environment

The dynamics of the true state vector are given by

$$\dot{\boldsymbol{r}}^i_o = \boldsymbol{\omega}^i_{\text{moon}} \times \boldsymbol{r}^i_o \tag{7}$$

$$\dot{\boldsymbol{r}}^i = \boldsymbol{v}^i \tag{8}$$

$$\dot{\boldsymbol{v}}^i = \boldsymbol{a}^i_{\text{grav}}(\boldsymbol{r}^i) + \boldsymbol{a}^i_{\text{thrust}}(\hat{\boldsymbol{a}}^\ell_{\text{com}}, \boldsymbol{p}_{\text{thrust}}) + \boldsymbol{\varepsilon}^i_{\text{grav}} + \boldsymbol{w}_a \tag{9}$$

$$\dot{\boldsymbol{q}}^\ell_i = \frac{1}{2}\begin{pmatrix} \boldsymbol{\omega}^\ell \\ 0 \end{pmatrix} \otimes \boldsymbol{q}^\ell_i \tag{10}$$

$$\dot{\boldsymbol{\omega}}^\ell = I_\ell^{-1}[-\boldsymbol{\omega}^\ell \times I_\ell \boldsymbol{\omega}^\ell + \boldsymbol{T}^\ell_{\text{torque}}(\hat{\boldsymbol{T}}^\ell_{\text{com}}, \boldsymbol{p}_{\text{torque}})] + \boldsymbol{w}_\alpha \tag{11}$$

Table 1 Linear covariance simulation states

	Quantity	Dynamics model
Landing site		
Inertial position	3	Lunar motion
Lander		
Inertial position/ velocity	6	Orbital motion (point mass + $J2$ gravity)
Attitude/attitude rate	6	Euler's equation
Sensors		
Accelerometers	9	First-order Markov bias, scale factor, and misalignment
Gyros	9	First-order Markov bias, scale factor, and misalignment
Velocimeter	9	First-order Markov bias, scale factor, and misalignment
TRN position sensor	9	First-order Markov bias, scale factor, and misalignment
TRN angles sensor	3	First-order Markov misalignment
Star camera	3	First-order Markov misalignment
Altimeter	3	First-order Markov bias
Actuators		
Thrust forces	9	First-order Markov bias, scale factor, and misalignment
Thrust torques	9	First-order Markov bias, scale factor, and misalignment
Environment		
Terrain map error	3	First-order Markov bias
Gravity model error	3	First-order Markov bias
Total	84	

$$\dot{p}_j = -p_j/\tau_j + w_{p_j}, \qquad j = 1, 2, 3, \ldots, n_p \tag{12}$$

$$\dot{\varepsilon}_k = -\frac{\varepsilon_k}{d_k/|\boldsymbol{v}^i|} + w_{\varepsilon_k}, \qquad k = 1, 2, 3, \ldots, n_\varepsilon \tag{13}$$

The angular velocity vector of the moon is denoted by $\boldsymbol{\omega}^i_{\text{moon}}$, and I_ℓ is the inertia of the lander. The gravitational acceleration, $\boldsymbol{a}^i_{\text{grav}}$, is derived from a point mass plus J_2 gravitational model [8] of the moon. All other perturbations in the moon's gravitational field are accounted for in the gravity error parameter $\boldsymbol{\varepsilon}_{\text{grav}}$. The control accelerations and torques from the thrusters, $\boldsymbol{a}^i_{\text{thrust}}$ and $\boldsymbol{T}^\ell_{\text{torque}}$, are defined in Eqs. (20) and (21) below. Unmodeled translational and rotational accelerations are accounted for as process noise, $\boldsymbol{w}_a$ and $\boldsymbol{w}_\alpha$, respectively, where

$$E[\boldsymbol{w}_a(t)\boldsymbol{w}_a^T(t')] = S_a\delta(t-t') \tag{14}$$

$$E[\boldsymbol{w}_\alpha(t)\boldsymbol{w}_\alpha^T(t')] = S_\alpha\delta(t-t') \tag{15}$$

Each sensor and actuator parameter p_j is modeled as a first-order Markov process with a steady-state variance $\sigma^2_{p_j}$, a time constant τ_j, and white noise w_{p_j} with variance

$$E[w_{p_j}(t)w_{p_j}(t')] = (\sigma^2_{p_j}/2\tau_j)\delta(t-t') \tag{16}$$

Similarly, each environment state ε_k is modeled as a first-order Markov process with a steady-state variance $\sigma^2_{\varepsilon_k}$, a correlation distance d_k, and white noise w_{ε_k} with variance

$$E[w_{\varepsilon_k}(t)w_{\varepsilon_k}(t')] = (\sigma^2_{\varepsilon_k}/2\tau_k)\delta(t-t') \tag{17}$$

B. Thruster Models

The thruster torque and acceleration error model parameters are scale factor, misalignment, and bias:

$$\boldsymbol{p}_{\text{thrust}} = (\boldsymbol{f}_{\text{thrust}}, \boldsymbol{\epsilon}_{\text{thrust}}, \boldsymbol{b}_{\text{thrust}})^T \tag{18}$$

$$\boldsymbol{p}_{\text{torque}} = (\boldsymbol{f}_{\text{torque}}, \boldsymbol{\epsilon}_{\text{torque}}, \boldsymbol{b}_{\text{torque}})^T \tag{19}$$

In terms of these parameters, the thruster acceleration model in Eq. (9) is given by

$$\boldsymbol{a}^i_{\text{thrust}}(\boldsymbol{a}^\ell_{\text{com}}, \boldsymbol{p}_{\text{thrust}}) = \mathcal{T}^i_\ell(\boldsymbol{q}^\ell_i)\delta\mathcal{T}(\boldsymbol{\epsilon}_{\text{thrust}})\{[I_{3\times3} + \text{Diag}(\boldsymbol{f}_{\text{thrust}})]\hat{\boldsymbol{a}}^\ell_{\text{com}} + \boldsymbol{b}_{\text{thrust}} + \boldsymbol{w}_{\text{thrust}}\} \tag{20}$$

and the thruster torque model in Eq. (11) is given by

$$\boldsymbol{T}^\ell_{\text{torque}}(\boldsymbol{T}^\ell_{\text{com}}, \boldsymbol{p}_{\text{torque}}) = \delta\mathcal{T}(\boldsymbol{\epsilon}_{\text{torque}})\{[I_{3\times3} + \text{Diag}(\boldsymbol{f}_{\text{torque}})]\hat{\boldsymbol{T}}^\ell_{\text{com}} + \boldsymbol{b}_{\text{torque}} + \boldsymbol{w}_{\text{torque}}\} \tag{21}$$

The flight computer algorithms for the thruster commands $\hat{\boldsymbol{a}}^\ell_{\text{com}}$ and $\hat{\boldsymbol{T}}^\ell_{\text{com}}$ are defined later, in Eqs. (63) and (64). The covariances of the thrust and torque actuation noise are given by

$$E[\boldsymbol{w}_{\text{thrust}}(t)\boldsymbol{w}^T_{\text{thrust}}(t')] = S_{w_{\text{thrust}}}\delta(t-t') \tag{22}$$

$$E[\boldsymbol{w}_{\text{torque}}(t)\boldsymbol{w}^T_{\text{torque}}(t')] = S_{w_{\text{torque}}}\delta(t-t') \tag{23}$$

C. Sensor Models

The lander inertial measurement unit (IMU) is a strap-down system with three orthogonal accelerometers to measure the components of the nongravitational acceleration of the lander and three orthogonal gyros to measure the angular velocity of the lander. The parameters for the accelerometer and gyro error models consist of scale-factor errors, misalignment errors, and bias errors:

$$\boldsymbol{p}_{\text{accel}} = (\boldsymbol{f}_{\text{accel}}, \boldsymbol{\epsilon}_{\text{accel}}, \boldsymbol{b}_{\text{accel}})^T \tag{24}$$

$$\boldsymbol{p}_{\text{gyro}} = (\boldsymbol{f}_{\text{gyro}}, \boldsymbol{\epsilon}_{\text{gyro}}, \boldsymbol{b}_{\text{gyro}})^T \tag{25}$$

In terms of these parameters, the output of the IMU in the lander frame is

$$\tilde{\boldsymbol{a}}^{\ell}_{\text{accel}} = [I_{3\times3} + \text{Diag}(\boldsymbol{f}_{\text{accel}})]\delta\mathcal{T}(\boldsymbol{\epsilon}_{\text{accel}})\mathcal{T}^{\ell}_{i}(\boldsymbol{q}^{\ell}_{i})\{\boldsymbol{a}^{i}_{\text{thrust}} + \boldsymbol{w}^{i}_{a}\} + \boldsymbol{b}_{\text{accel}} + \boldsymbol{w}_{\text{accel}} \tag{26}$$

$$\tilde{\boldsymbol{\omega}}^{\ell} = [I_{3\times3} + \text{Diag}(\boldsymbol{f}_{\text{gyro}})]\delta\mathcal{T}(\boldsymbol{\epsilon}_{\text{gyro}})\boldsymbol{\omega}^{\ell} + \boldsymbol{b}_{\text{gyro}} + \boldsymbol{\eta}_{\text{gyro}} \tag{27}$$

where the covariances of the accelerometer noise and gyro noise are

$$E[\boldsymbol{\eta}_{\text{accel}}(t)\boldsymbol{\eta}^{T}_{\text{accel}}(t')] = S_{\eta_{\text{accel}}}\delta(t-t') \tag{28}$$

$$E[\boldsymbol{\eta}_{\text{gyro}}(t)\boldsymbol{\eta}^{T}_{\text{gyro}}(t')] = S_{\eta_{\text{gyro}}}\delta(t-t') \tag{29}$$

The star camera is used to measure the three-axis orientation of the lander. The star-camera error model has only one parameter, the three-dimensional uncertainty in the alignment of the star camera with respect to the lander frame of reference. Thus, $\boldsymbol{p}_{\text{starcam}} = \boldsymbol{\epsilon}_{\text{starcam}}$. The output of the star camera is modeled as

$$\tilde{\boldsymbol{q}}^{\text{starcam}}_{i} = \delta\boldsymbol{q}(\boldsymbol{\nu}_{\text{starcam}}) \otimes \delta\boldsymbol{q}(\boldsymbol{\epsilon}_{\text{starcam}}) \otimes \bar{\boldsymbol{q}}^{\text{starcam}}_{\ell} \otimes \boldsymbol{q}^{\ell}_{i} \tag{30}$$

where the covariance of the measurement noise $\boldsymbol{\nu}_{\text{starcam}}$ is given by

$$E[\boldsymbol{\nu}_{\text{starcam}}(t_m)\boldsymbol{\nu}^{T}_{\text{starcam}}(t_n)] = R_{\nu_{\text{starcam}}}\delta_{mn} \tag{31}$$

The lander altimeter measures the altitude of the lander above the lunar terrain. The error model parameters include a scale factor, a bias, and a terrain elevation knowledge error, $\boldsymbol{p}_{\text{alt}} = (f_{\text{alt}}, b_{\text{alt}}, b_{\text{terrain}})^T$. The altitude measurement is modeled as

$$\tilde{h}_{\text{alt}} = (1 + f_{\text{alt}})\{|\boldsymbol{r}^{i}| - h_{\text{terrain}} - \rho_{\text{moon}}\} + b_{\text{alt}} + b_{\text{terrain}} + \nu_{\text{alt}} \tag{32}$$

where h_{terrain} is the altitude of the terrain, ρ_{moon} is the spherical radius of the moon, and ν_{alt} represents white measurement noise with variance

$$E[\nu_{\text{alt}}(t_m)\nu_{\text{alt}}(t_n)] = \sigma^{2}_{\nu_{\text{alt}}}\delta_{mn} \tag{33}$$

The lander velocimeter provides a three-dimensional measurement of the surface-relative velocity in the instrument frame. The parameters used in the velocimeter error model are scale factor, bias, and an unknown misalignment of the instrument, $\boldsymbol{p}_{\text{vel}} = (\boldsymbol{f}_{\text{vel}}, \boldsymbol{b}_{\text{vel}}, \boldsymbol{\epsilon}_{\text{vel}})^T$. In terms of these parameters, the velocimeter model can be written

$$\tilde{\boldsymbol{v}}^{\text{vel}}_{\text{rel}} = [I_{3\times3} + \text{Diag}(\boldsymbol{f}_{\text{vel}})]\delta\mathcal{T}(\boldsymbol{\epsilon}_{\text{vel}})\bar{\mathcal{T}}^{\text{vel}}_{\ell}\mathcal{T}^{\ell}_{i}(\boldsymbol{q}^{\ell}_{i})\{\boldsymbol{v}^{i} - \boldsymbol{\omega}^{i}_{\text{moon}} \times \boldsymbol{r}^{i}\} + \boldsymbol{b}_{\text{vel}} + \boldsymbol{\nu}_{\text{vel}} \tag{34}$$

where the covariance of the measurement noise $\boldsymbol{\nu}_{\text{vel}}$ is given by

$$E[\boldsymbol{\nu}_{\text{vel}}(t_m)\boldsymbol{\nu}^{T}_{\text{vel}}(t_n)] = R_{\nu_{\text{vel}}}\delta_{mn} \tag{35}$$

The TRN angle sensor provides line-of-sight information by measuring the pixel location of known landmarks on the surface. The only error model parameter associated with this sensor is an unknown misalignment of the sensor with the frame of the lander, or $\boldsymbol{p}_{\text{trnang}} = \boldsymbol{\epsilon}_{\text{trnang}}$. The model for the focal plane measurement [9] of a landmark is given by

$$\tilde{\boldsymbol{l}}^{\text{trnang}} = \begin{pmatrix} l_x/l_z \\ l_y/l_z \end{pmatrix} + \boldsymbol{\nu}_{\text{trnang}} \tag{36}$$

where the relative position of the landmark, $\boldsymbol{l}^{\text{trn}}_{\text{los}} = [l_x, l_y, l_z]$, in the TRN frame is given by

$$\tilde{\boldsymbol{l}}^{\text{trn}}_{\text{los}} = \delta\mathcal{T}(\boldsymbol{\epsilon}_{\text{trnang}})\bar{\mathcal{T}}^{\text{trn}}_{\ell}\mathcal{T}^{\ell}_{i}(\boldsymbol{q}^{\ell}_{i})\{-\boldsymbol{r}^{i} + (\boldsymbol{r}^{i}_{o} + \Delta\boldsymbol{r}^{i}_{l} + \mathcal{T}^{i}_{s}\boldsymbol{e}^{s}_{\text{map}})\} \tag{37}$$

and $\boldsymbol{\nu}_{\text{trnang}}$ represents white noise with a covariance

$$E[\boldsymbol{\nu}_{\text{trnang}}(t_m)\boldsymbol{\nu}^{T}_{\text{trnang}}(t_n)] = R_{\nu_{\text{trnang}}}\delta_{mn} \tag{38}$$

The vector $\Delta\boldsymbol{r}^{i}_{l}$ used in Eqs. (37) and (39) represents a position vector from the landing objective to the landmark.

The second possible configuration of the TRN sensor includes a method to determine the position vector of the lander relative to the landing objective. The parameters for this model include a scale factor, a bias, and an unknown misalignment in the orientation of the sensor, $\boldsymbol{p}_{\text{trnpos}} = (\boldsymbol{f}_{\text{trnpos}}, \boldsymbol{b}_{\text{trnpos}}, \boldsymbol{\epsilon}_{\text{trnpos}})^T$. The model for the measurement of the lander's position in the TRN frame in terms of these parameters is

$$\tilde{\boldsymbol{r}}^{\text{trn}}_{\Delta r} = [I_{3\times3} + \text{Diag}(\boldsymbol{f}_{\text{trnpos}})]\delta\mathcal{T}(\boldsymbol{\epsilon}_{\text{trnpos}})\bar{\mathcal{T}}^{\text{trn}}_{\ell}\mathcal{T}^{\ell}_{i}(\boldsymbol{q}^{\ell}_{i})\{-\boldsymbol{r}^{i} + (\boldsymbol{r}^{i}_{o} + \Delta\boldsymbol{r}^{i}_{l} + \mathcal{T}^{i}_{s}\boldsymbol{e}^{s}_{\text{map}})\} + \boldsymbol{b}_{\text{trnpos}} + \boldsymbol{\nu}_{\text{trnpos}} \tag{39}$$

where the covariance of the measurement noise $\boldsymbol{\nu}_{\text{trnpos}}$ is given by

$$E[\boldsymbol{\nu}_{\text{trnpos}}(t_m)\boldsymbol{\nu}^{T}_{\text{trnpos}}(t_n)] = R_{\nu_{\text{trnpos}}}\delta_{mn} \tag{40}$$

III. Flight Algorithm Models

The navigation state is defined by an $\hat{n}$-dimensional vector:

$$\hat{\boldsymbol{x}} = (\hat{\boldsymbol{x}}_o, \hat{\boldsymbol{x}}_\ell, \hat{\boldsymbol{p}}, \hat{\boldsymbol{\varepsilon}})^T \tag{41}$$

It is composed of three states for the landing objective, nine states for the lander, $\hat{n}_p = 63$ parameter states, and $\hat{n}_\varepsilon = 6$ environment states:

$$\hat{\boldsymbol{x}}_o = (\hat{\boldsymbol{r}}^{i}_{o}) \tag{42}$$

$$\hat{\boldsymbol{x}}_\ell = (\hat{\boldsymbol{r}}^{i}, \hat{\boldsymbol{v}}^{i}, \hat{\boldsymbol{q}}^{\ell}_{i})^T \tag{43}$$

$$\hat{\boldsymbol{p}} = (\hat{\boldsymbol{p}}_s, \hat{\boldsymbol{p}}_a)^T \tag{44}$$

$$\hat{\boldsymbol{\varepsilon}} = (\hat{\boldsymbol{\varepsilon}}^{s}_{\text{map}}, \hat{\boldsymbol{\varepsilon}}^{i}_{\text{grav}})^T \tag{45}$$

The angular velocity of the lander is omitted because the attitude model operates in model replacement mode [9], in which the gyro measurements replace the Euler equations that would otherwise model the dynamics of the angular velocity state.

A. Navigation Algorithm

The navigation state propagation equations are given by

$$\dot{\hat{\boldsymbol{r}}}^{i}_{o} = \boldsymbol{\omega}_{\text{moon}} \times \hat{\boldsymbol{r}}^{i}_{o} \tag{46}$$

$$\dot{\hat{\boldsymbol{r}}}^{i} = \hat{\boldsymbol{v}}^{i} \tag{47}$$

$$\dot{\hat{\boldsymbol{v}}}^{i} = \hat{\boldsymbol{a}}^{i}_{\text{grav}}(\hat{\boldsymbol{r}}^{i}) + \hat{\boldsymbol{\varepsilon}}^{i}_{\text{grav}} + \hat{\boldsymbol{a}}^{i}_{\text{nongrav}}(\tilde{\boldsymbol{a}}^{\ell}_{\text{accel}}, \hat{\boldsymbol{p}}_{\text{accel}}) \tag{48}$$

$$\dot{\hat{\boldsymbol{q}}}^{\ell}_{i} = \frac{1}{2}\begin{pmatrix} \hat{\boldsymbol{\omega}}_{\text{comp}}(\tilde{\boldsymbol{\omega}}^{\ell}, \hat{\boldsymbol{p}}_{\text{gyro}}) \\ 0 \end{pmatrix} \otimes \hat{\boldsymbol{q}}^{\ell}_{i} \tag{49}$$

$$\dot{\hat{p}}_k = -(\hat{p}_k/\hat{\tau}_k), \qquad k = 1, 2, 3, \ldots, \hat{n}_p \tag{50}$$

$$\dot{\hat{\varepsilon}}_k = -\frac{\hat{\varepsilon}_k}{\hat{d}_k/|\hat{\boldsymbol{v}}^{i}|}, \qquad k = 1, 2, 3, \ldots, \hat{n}_\varepsilon \tag{51}$$

The accelerometer measurements of the accelerations due to the thrusters and nongravitational disturbances are corrected using the best estimates of the accelerometer error model parameters and used directly in the propagation of the lander's position and velocity:

$$\hat{\boldsymbol{a}}^{i}_{\text{nongrav}}(\tilde{\boldsymbol{a}}^{\ell}_{\text{accel}}, \hat{\boldsymbol{p}}_{\text{accel}}) = \mathcal{T}^{i}_{\ell}(\hat{\boldsymbol{q}}^{i}_{\ell})\delta\mathcal{T}(-\hat{\boldsymbol{\epsilon}}_{\text{accel}})\{[I_{3\times3} - \text{Diag}(\hat{\boldsymbol{f}}_{\text{accel}})]\tilde{\boldsymbol{a}}^{\ell}_{\text{accel}} - \hat{\boldsymbol{b}}_{\text{accel}}\} \tag{52}$$

Similarly, the corrected measurement of the angular velocity is used to propagate the quaternion of the lander:

$$\hat{\boldsymbol{\omega}}_{\text{comp}}(\tilde{\boldsymbol{\omega}}^{\ell}, \hat{\boldsymbol{p}}_{\text{gyro}}) = \delta\mathcal{T}(-\hat{\boldsymbol{\epsilon}}_{\text{gyro}})\{[I_{3\times 3} - \text{Diag}(\hat{\boldsymbol{f}}_{\text{gyro}})]\tilde{\boldsymbol{w}}^{\ell}_{\text{gyro}} - \hat{\boldsymbol{b}}_{\text{gyro}}\} \tag{53}$$

For gravitational acceleration, $\hat{\boldsymbol{a}}^{i}_{\text{grav}}$ is a point mass plus J_2 gravity model [8].

These propagation equations can be written in the compact form

$$\dot{\hat{\boldsymbol{x}}} = \hat{\boldsymbol{f}}(\hat{\boldsymbol{x}}, \tilde{\boldsymbol{y}}, t) \tag{54}$$

where $\tilde{\boldsymbol{y}} = (\tilde{\boldsymbol{a}}^{\ell}_{\text{accel}}, \tilde{\boldsymbol{w}}^{\ell}_{\text{gyro}})^T$ is the output of the IMU as defined in Eqs. (26) and (27). Linearizing this system of equations leads to the navigation state covariance propagation equations:

$$\dot{\hat{P}} = \hat{F}_{\hat{x}}\hat{P} + \hat{P}\hat{F}_{\hat{x}} + \hat{S}_{\eta} + \hat{S}_{w} \tag{55}$$

where $\hat{F}_{\hat{x}}$ is the partial of $\hat{\boldsymbol{f}}$ with respect to $\hat{\boldsymbol{x}}$. These partial derivatives, the state process noise covariance $\hat{S}_{w}$, and the covariance $\hat{S}_{\eta}$ due to gyro and accelerometer noise are given in Appendix B.

Note that "modified" states [10] are used in deriving this covariance propagation equation. The four-dimensional quaternion state $\hat{\boldsymbol{q}}^{\ell}_{i}$ is replaced by three-dimensional rotation vector states $\hat{\boldsymbol{\theta}}^{\ell}_{i}$, and the quaternion kinematics are replaced by the Bortz equation [9]. Thus, quaternion errors $\delta\hat{\boldsymbol{q}}^{\ell}_{i}$ are replaced by a three-dimensional small-angle rotation vector $\delta\hat{\boldsymbol{\theta}}^{\ell}_{i}$ and the linearized Bortz equation is used to derive the attitude covariance propagation equations.

All the navigation state update equations

$$\delta\hat{\boldsymbol{x}}_{m} = \hat{K}(t_m)[\tilde{\boldsymbol{z}}_{m} - \hat{\boldsymbol{h}}(\hat{\boldsymbol{x}}_{m}, t_m)] \tag{56}$$

are additive:

$$\hat{\boldsymbol{x}}^{+}_{m} = \hat{\boldsymbol{x}}^{-}_{m} + \delta\hat{\boldsymbol{x}}_{m} \tag{57}$$

with the exception of the attitude updates, which are implemented as small quaternion rotations:

$$(\hat{\boldsymbol{q}}^{\ell}_{i})^{+} = \delta\boldsymbol{q}(\delta\hat{\boldsymbol{\theta}}^{\ell}_{i}) \otimes (\hat{\boldsymbol{q}}^{\ell}_{i})^{-} \tag{58}$$

When processing altimeter, velocimeter, angular TRN, and positional TRN measurements, $\tilde{\boldsymbol{z}}_{m}$ is simply the output of the sensor and $\hat{\boldsymbol{h}}(\hat{\boldsymbol{x}}_{m}, t_m)$ is the estimate of the measurement based on the error models given in Eqs. (32), (34), (36), and (39), respectively.

When processing star-camera data, $\tilde{\boldsymbol{z}}_{m}$ is a derived measurement [9] calculated from

$$\begin{pmatrix} \frac{1}{2}\tilde{\boldsymbol{z}}_{m} \\ 1 \end{pmatrix} = \tilde{\boldsymbol{q}}^{\text{starcam}}_{i} \otimes \hat{\boldsymbol{q}}^{i}_{\ell} \otimes \bar{\boldsymbol{q}}^{\ell}_{\text{starcam}} \otimes \delta\boldsymbol{q}(-\hat{\boldsymbol{\epsilon}}_{\text{starcam}}) \tag{59}$$

For a standard Kalman filter, the flight computer estimate of the derived star-camera measurement is

$$\hat{\boldsymbol{h}}(\hat{\boldsymbol{x}}_{m}, t_m) = \hat{\mathcal{T}}^{\text{starcam}}_{\ell}\delta\hat{\boldsymbol{\theta}}^{\ell}_{i} + \hat{\boldsymbol{\epsilon}}_{\text{starcam}} \tag{60}$$

where $\hat{\boldsymbol{\epsilon}}_{\text{starcam}}$ is the flight computer value of the star-camera misalignment.

The navigation state covariance update equation is given by [11]

$$\hat{P}(t^{+}_{m}) = [I - \hat{K}(t_m)\hat{H}_{\hat{x}}(t_m)]\hat{P}(t^{-}_{m})[I - \hat{K}(t_m)\hat{H}_{\hat{x}}(t_m)]^T + \hat{K}(t_m)\hat{R}_{v}(t_m)\hat{K}^T(t_m) \tag{61}$$

where the Kalman gain $\hat{K}(t_m)$ is given by

$$\hat{K}(t_m) = \hat{P}(t^{-}_{m})\hat{H}^T_{\hat{x}}(t_m)[\hat{H}_{\hat{x}}(t_m)\hat{P}(t^{-}_{m})\hat{H}^T_{\hat{x}}(t_m) + \hat{R}_{v}(t_m)]^{-1} \tag{62}$$

The measurement sensitivity matrices $\hat{H}_{\hat{x}}$ and the measurement covariance matrices $\hat{R}_{v}$ for the star camera, altimeter, velocimeter, and the TRN sensors are given in Appendix B.

B. Translational and Rotational Control Algorithms

A simple proportional–derivative controller is used to control the position and attitude of the lander so that it follows a predefined nominal trajectory $(\bar{\boldsymbol{r}}^{i}(t), \bar{\boldsymbol{v}}^{i}(t), \bar{\boldsymbol{q}}_{i}(t))$. The commanded acceleration and the torque are calculated using the following control laws:

$$\hat{\boldsymbol{a}}^{\,i}_{\text{com}}(\hat{\boldsymbol{x}}, t) = \hat{K}_{r}[\bar{\boldsymbol{r}}^{i}(t) - \hat{\boldsymbol{r}}^{i}] + \hat{K}_{v}[\bar{\boldsymbol{v}}^{i}(t) - \hat{\boldsymbol{v}}^{i}] \tag{63}$$

$$\hat{\boldsymbol{T}}^{\,\ell}_{\text{com}}(\hat{\boldsymbol{x}}, t) = \hat{K}_{\theta}\Delta\hat{\boldsymbol{\theta}}_{\text{com}} + \hat{K}_{\omega}[\bar{\boldsymbol{\omega}}^{\ell}(t) - \hat{\boldsymbol{\omega}}^{\ell}] \tag{64}$$

where $\hat{K}_{r}$, $\hat{K}_{v}$, $\hat{K}_{\theta}$, and $\hat{K}_{\omega}$ are controller gains, and $\Delta\hat{\boldsymbol{\theta}}_{\text{com}}$ represents attitude control error as defined by

$$\begin{pmatrix} \frac{1}{2}\Delta\hat{\boldsymbol{\theta}}_{\text{com}} \\ 1 \end{pmatrix} = \bar{\boldsymbol{q}}^{i}_{i}(t) \otimes \hat{\boldsymbol{q}}^{i}_{\ell} \tag{65}$$

IV. Sensor Errors, Environment Errors, and Nominal Trajectory

The baseline sensor suite considered in this paper is the sensor suite proposed by NASA's Autonomous Landing and Hazard Avoidance Technology (ALHAT) project [5,12,13]. It consists of gyros, accelerometers, a star camera, an altimeter, and a velocimeter. The values of the gyro, accelerometer, and star-camera model parameters and operating regimes are consistent with the ALHAT project data [4,5] and are given in Table 2. Accelerometer data are processed only during maneuvers to avoid the cumulative effects of undesired accelerometer bias and noise. The values of the altimeter and velocimeter model parameters are also consistent with the ALHAT project data [4,5] and are given in Table 3. A time constant of $\tau = \infty$ is assumed unless explicitly stated otherwise.

The values of the baseline environment model parameters are shown in Table 4. The random nongravitational accelerations [15] produce a 500 m 3-σ along-track uncertainty per one-half orbit. The gravity model error [14], 60 mGal 3-σ, assumes that the central force and J_2 are accounted for explicitly and produces an approximately 6 km 3-σ along-track uncertainty per one-half orbit. Because it is known from the Apollo missions that gravity error compensation can substantially reduce the effect of this error source [6], the baseline gravity error can optionally be reduced to 6 mGal 3-σ. The baseline initial position and velocity navigation errors at deorbit are also consistent with those used by ALHAT [4].[‡] The sensitivity of landing navigation performance to these initial navigation errors is also briefly investigated.

Two ALHAT nominal trajectories, a *high* trajectory and a *low* trajectory, were selected for analysis and are shown in Fig. 2. The high trajectory has a final vertical descent that begins at 3 km, and the low trajectory has a final vertical descent that begins at 200 m. In both cases, deorbit occurs at a 100 km altitude. Powered descent initiation (PDI) occurs approximately 312 km uprange of and 19.2 km above the landing-site altitude for the low trajectory and approximately 300 km uprange of and 17 km above the landing-site altitude for the high trajectory. The high trajectory has the capability of removing 2.5 km of trajectory dispersion at the beginning of the vertical descent (with a cost of 3% of the total Δv). The low trajectory must remove trajectory dispersions further uprange of the landing site.

V. Inertial Navigation Analysis

To gain a better understanding of the effects of gyro error, accelerometer error, star-camera error, initial state error, gravity model error, nongravitational disturbances, and altimeter and velocimeter error on navigation performance, a preliminary LinCov analysis was conducted. The objective of the analysis was to get an order-of-magnitude feel for how these errors affect navigation

[‡]Personal notes of E. Schiesser, 2006 ("Navigation Error Covariance Matrices for CEV and LSAM lunar orbit GN&C Analysis").

Table 2 Gyro, accelerometer, and star-camera baseline error model parameters consistent with the ALHAT project data [4,5]

Sensor	Operating range	Model error (1-σ)	Comments
Star camera	Deorbit to landing	Misalignment: 50 arcsecond/axis Measurement noise: 50 arcsecond/axis	0.5 Hz
Accelerometers	During deorbit maneuver and PDI through landing	Bias: 30 μg Scale factor: 66 ppm Random walk: 0.00017 m/s/$\sqrt{s}$ Misalignment: 20 arcsecond	0.5 Hz
Gyros	Deorbit through landing	Bias: 0.02 deg/hr Scale factor: 1.6 ppm Angle random walk: 0.00005 deg/$\sqrt{s}$ Misalignment: 20 arcsecond	0.5 Hz

Table 3 Baseline altimeter and velocimeter error model parameters consistent with the ALHAT project data [4,5]

Sensor	Operating range	Model error (1-σ)	Comments
Altimeter		Bias: 0.5 m ($\tau = 100$ s) Scale factor: 0.1% ppm ($\tau = 100$ s)	0.5 Hz Terrain uncertainty is 33 m with 10 m correlation distance for range >0.5 km (3.3 m for range <0.5 km)
	20–120 km	Measurement noise: 10 m	
	2–20 km	Measurement noise: 5 m	
	0.01–2 km	Measurement noise: 1 m	
Velocimeter	10 m–2 km	Bias: 0.1 m/s ($\tau = 100$ s) Scale factor: 0.1% ppm ($\tau = 100$ s) Measurement noise: 0.5 m/s Misalignment: 50 arcsecond	0.5 Hz

Table 4 Baseline environment error model parameters

Error source	Model error (1-σ)	Comments
Intermediate initial position/velocity error [4]‡	1500 m downrange, 0.047 m/s downrange rate 200 m cross track, 0.2 m/s cross-track rate 50 m altitude, 1.5 m/s altitude rate	−0.9 correlation between downrange and altitude rate, −0.9 correlation between downrange rate and altitude
Gravity [14]	20 mGal/2 mGal w/wo gravity error compensation 400 km correlation distance	Equivalent to approximately 2 km/0.2 km along-track error (per 1/2 orbit)
Random accelerations [15]	Process noise: 0.4 mm/s/$\sqrt{s}$	Equivalent to approximately 500 m along-track error (per 1/2 orbit)

performance. The results are relatively independent of the particular lunar-landing reference trajectory and serve as a guide to understanding the relative importance and magnitude of a wide variety of navigation error sources.

Table 5 shows the effect of several error sources on inertial navigation performance at PDI, the end of the braking burn, and landing. The data in each row of the table show the impact of only the indicated error source, with all other error sources and measurement types turned off. Nongravitational disturbances, *low* initial state uncertainties, and the total effect of gyro, accelerometer, and star-camera errors produce navigation errors on the order of 100–400 m 3-σ at PDI and 300–700 m 3-σ at touchdown. Gravity model errors produce approximately 4–6 km of navigation error, and the *high* initial state uncertainties produce more than 40 km of error, all of which is primarily in the downrange direction. The ALHAT program is currently using the high and low initial position errors to represent the worst- and best-case state uncertainties for low-lunar-orbit navigation.

Table 6 shows the benefit of altimeter and velocimeter measurements and the effect of operating these instruments at different altitudes. Column 2 shows the inertial navigation performance without the altimeter or the velocimeter. Column 3 shows the effect of adding just the altimeter, and column 4 shows the effect of adding both the altimeter and the velocimeter. In column 5, the effect of adding gravity error compensation is shown. The data show that navigation performance is not significantly improved by operating the altimeter/velocimeter at altitudes much higher than 20 km. There is, however, a significant advantage in operating the altimeter in the 2–20 km altitude range, in which timely improvements in altitude and downrange knowledge can be used for the braking maneuver. The downrange improvement is achieved through orbital downrange-altitude error correlations. The velocimeter provides some improvement in velocity knowledge, but does not provide a significant improvement in position knowledge and is thus only needed at the lower altitudes (<2 km) to determine the horizontal surface velocity to prepare for landing. Notice also that a significant reduction in landing error is achieved when gravity error compensation is used in conjunction with the low initial state errors.

These results were obtained to gain a general understanding of the relative importance of a wide range of navigation error sources. Based on these results, we were able to narrow the scope of the analysis and focus on the more practical navigation solutions. In particular, we make the following additional assumptions: 1) the altimeter operating range is 0.01–20.0 km, 2) the velocimeter operating range is 0.01–2.0 km, and 3) the *high* initial state errors are eliminated from the analysis space.

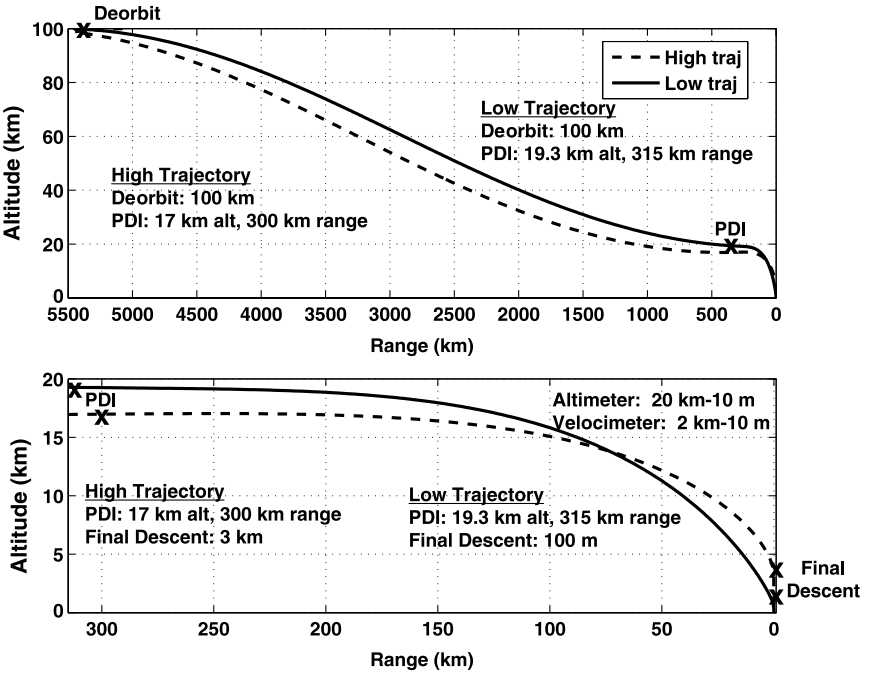

Fig. 2 Nominal/reference high and low trajectories selected for analysis.

The performance of the baseline navigation system and the associated sensitivity analysis are summarized in Figs. 3–6. Results for the high trajectory are shown in Figs. 3 and 4, and results for the low trajectory are shown in Figs. 5 and 6. Each figure shows the total inertial navigation position error as a function of time and the contribution from each error source to the total as a function of time. The individual error sources are 1) gravity model errors, 2) nongravitational disturbances, 3) initial state uncertainties, and 4) altimeter, velocimeter, gyro, and accelerometer instrument errors. The rss of the individual component errors equals the total navigation position error, and each component error is proportional to the error source. Therefore, if gravity model errors or initial state uncertainties are doubled, their individual contributions to the total navigation error will double. If their errors are halved, their contributions to the total will be halved. If a particular component error is a large fraction of the total error, doubling or halving the error source will approximately double or halve the total. Thus, these figures can be used by system designers to determine when a better sensor or subsystem may provide significant improvement in the overall system or when a less expensive, less accurate sensor or subsystem may suffice without comprising the overall performance of the system. In all cases, the nongravitational disturbances have little impact on the total navigation error.

Table 5 Effects of individual error sources on inertial navigation performance at PDI, the end of the braking maneuver, and landing

Error source	Inertial	Nav error	3-σ
	PDI	Braking	Landing
Accelerometer, gyros, and star camera	100 m	400 m	700 m
Gravity model			
20 mGal (1-σ), 400 m correlation distance	4 km	5 km	6 km
Nongravitational disturbances			
0.4 mm/s/$\sqrt{s}$ (1-σ)	350 m	450 m	500 m
High initial pos/vel errors (1-σ)			
10,000 m downrange, 0.28 m/s downrange rate			
1000 m cross track, 1 m/s cross-track rate	41 km	40 km	40 km
300 m altitude, 9.5 m/s altitude rate			
−0.9 correlation			
Low initial pos/vel errors (1-σ)			
86 m downrange, 0.0095 m/s downrange rate			
70 m cross track, 0.07 m/s cross-track rate	400 m	360 m	350
10 m altitude rate, 0.0814 m/s altitude rate			
−0.9 correlation			

For the baseline trajectories, the final landing uncertainties are approximately 1 km 3-σ. These uncertainties are reduced to 500–600 m 3-σ when using low initial state errors and gravity error compensation. Although this is good performance, it will not be sufficient to meet the 100 m 3-σ relative position knowledge requirement and justifies some form of terrain- or landing-site-relative navigation.

The altimeter plays a significant role in reducing the navigation knowledge error before PDI and during the braking maneuver. Sufficient time should be allowed before PDI to extract as much information from the altimeter data as possible. Information in the downrange position is obtained through correlations between altitude uncertainties and downrange uncertainties. Altimeter performance has a larger impact on the overall navigation performance for the baseline intermediate initial state uncertainty case because the error that the altimeter can remove, the downrange error, is much larger than the error that the altimeter cannot remove, the cross-track error. Altimeter performance has less of an impact on the cases with low state uncertainty because the downrange component is comparable to the cross-track component.

The baseline navigation uncertainties before PDI and altimeter acquisition are on the order of 10 km 3-σ. This knowledge error is predominantly due to initial state uncertainties at deorbit and is predominantly in the downrange direction. The uncertainty translates roughly into 10 km 3-σ of trajectory dispersion from the nominal that must be taken out during the braking maneuver. However, because the dispersion is also predominantly in the downrange direction, most of the dispersion can be eliminated by simply adjusting the remaining time of flight. The residual cross-track and altitude dispersions can be removed by maneuvering the lander as navigation accuracy improves.

With gravity error compensation and low initial state uncertainties, the navigation error before PDI and altimeter acquisition is reduced to 1 km 3-σ. This is a tenfold improvement over the baseline. The remaining error is predominantly due to residual gravity model

Table 6 Inertial navigation performance in kilometers (3-σ) at PDI, the end of the braking burn, and landing for various sensor configurations

	Gyros, accels, star cam, grav error, and disturbances	+Altimeter	+Velocimeter	+Gravity error compensation
Altimeter/velocimeter operating altitude		High initial state errors		
$h < 120$ km	41, 40, 40	26, 2.1, 1.8	1.6, 1.2, 1.2	1.5, 1.0, 1.0
$h < 20$ km	41, 40, 40	26, 2.2, 1.8	3.0, 1.5, 1.5	2.9, 1.3, 1.3
$h < 2$ km	41, 40, 40	41, 40, 3.4	41, 40, 2.8	41, 40, 2.3
Altimeter/velocimeter operating altitude		Low initial state errors		
$h < 120$ km	4.1, 5.4, 5.9	0.78, 0.83, 0.92	0.74, 0.74, 0.74	0.35, 0.34, 0.34
$h < 20$ km	4.1, 5.4, 5.9	0.95, 0.93, 1.0	0.92, 0.86, 0.86	0.39, 0.38, 0.38
$h < 2$ km	4.1, 5.4, 5.9	4.1, 5.4, 1.9	4.1, 5.4, 1.9	0.43, 0.55, 0.40

errors and initial state uncertainties and is distributed nearly equally in the downrange and cross-track directions. Again, the downrange dispersion component can be removed by adjusting the flight time, and the residual cross-track and attitude dispersions can be removed by maneuvering the lander as navigation accuracy improves.

Velocimeter performance is not a factor for the high trajectory because it is used only during the final vertical descent, during which the altimeter is effectively providing the same data. In contrast, the low trajectory uses the horizontal velocity data before the vertical descent begins. Velocimeter performance is an important factor for the low trajectory.

VI. Terrain-Relative Navigation Analysis

The objective of the LinCov terrain-relative navigation analysis is to understand the relative importance of several terrain-relative navigation error sources and to determine the minimum TRN requirements to achieve a 100 m 3-σ landing precision requirement. The TRN requirements include sensor performance requirements, operating range requirements (altitudes, velocities, orientation, and rotation rates), and a priori terrain mapping mission requirements. Once the minimum requirements are determined, the requirements can be tightened as needed to improve overall system safety, robustness, and fuel performance. For this research, two generic TRN options were considered: 1) a TRN system that determines the position relative to the terrain, and 2) a TRN system that determines relative angles or bearing measurements to surface features. The error models used in the LinCov analysis for these two options are described next.

It is important to point out that there are two competing interests pulling the operation of the TRN in opposite directions. To remove trajectory dispersions and minimize their effect on fuel performance, it is desirable to have TRN function early in the descent trajectory. This in turn requires the TRN to operate at higher altitudes and in general requires more terrain to be mapped at distances far from the landing site. On the other hand, to meet the 100 m 3-σ knowledge error at landing, it is desirable to have the TRN function as late in the descent trajectory as possible. A simpler design is required if the TRN operates late in the trajectory over a small altitude/velocity range and at lower altitudes when the landing site is potentially in the field of view and a priori terrain mapping requirements are minimal. In addition, there is no need for the TRN to overperform to compensate for the cumulative effect of the IMU errors. Qualitatively, there appears to be a middle ground in which the TRN can function early enough to accommodate dispersion control and yet late enough so as not be overburdened with excessive instrument performance requirements, terrain mapping requirements, and operating range requirements.

A. Terrain-Relative Navigation Error Models

In Fig. 7, the two major components of the LinCov TRN error models, instrument error and map error, are illustrated. The map

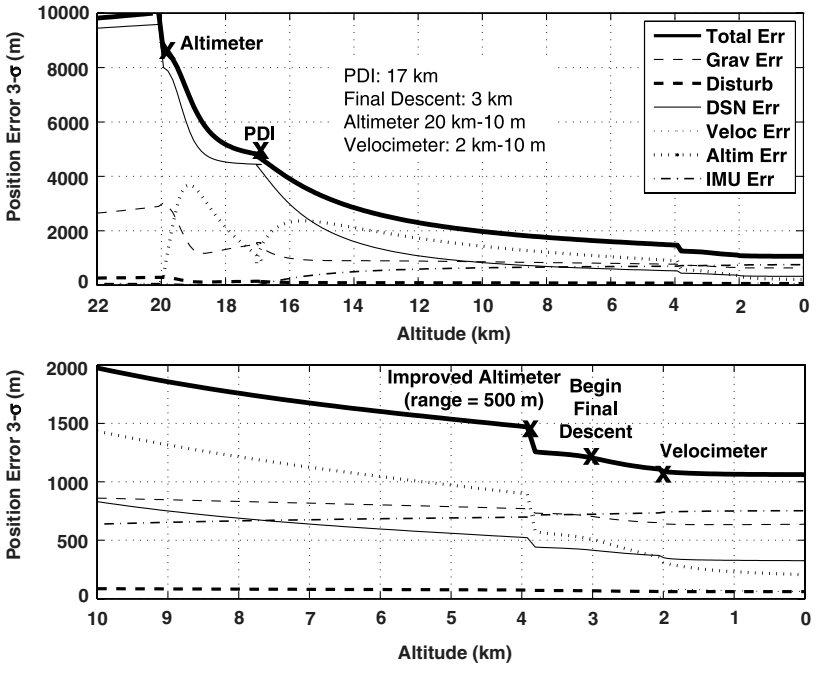

Fig. 3 Total inertial navigation position uncertainty and individual components (high trajectory).

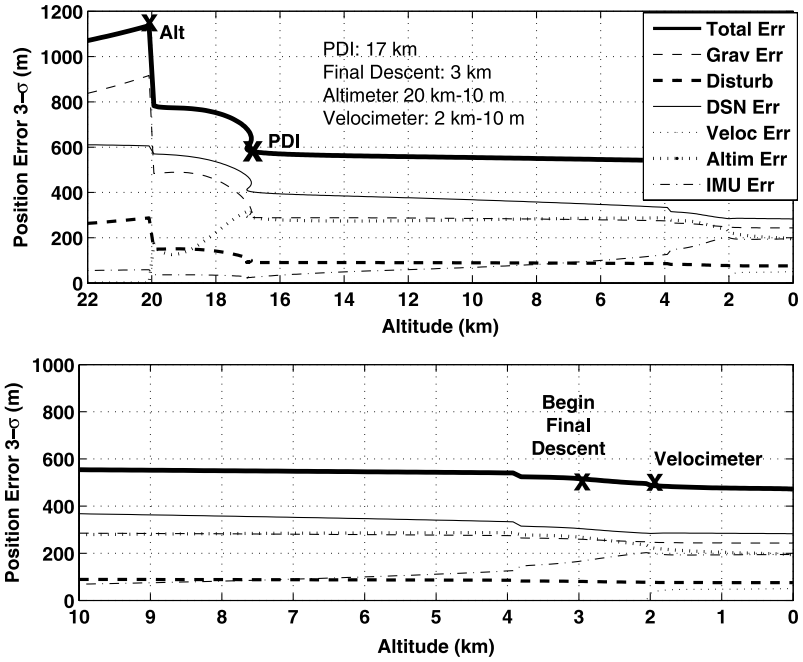

Fig. 4 Total inertial navigation position uncertainty and individual components with gravity model error compensation and low initial state uncertainties (high trajectory).

error, which is directly related to map resolution, is a measure of how well the positions of surface features are known relative to the landing site in the map frame. For this analysis, the map error was assumed to be 300 m 3-σ for surface features located more than 10 km from the landing site and 30 m 3-σ for features located less than 10 km from the landing site. Although this two-tiered terrain mapping error model is somewhat simplified relative to what would be provided from a surface mapping mission, it is complex enough to help in understanding the impact on TRN performance and TRN trends. An additional error, the map-tie error, or the uncertainty of the inertial location of the landing site, is assumed to be 100 m 3-σ in the north–east directions and 10 m 3-σ in the radial direction. This uncertainty, however, does not play a major role in TRN performance.

The numerical values for the TRN instrument error model parameters are shown in Table 7. Two generic models are shown. The first model assumes that the TRN instrument provides terrain-relative position vectors, and the error model is defined by the accuracy of the position measurements. The second model assumes that the TRN instrument provides angles or bearing measurements to surface features and is defined by the accuracy of the angle measurements. Instead of specifying the TRN instrument accuracy and then using LinCov to determine the relative navigation error at landing, we used the LinCov in a novel iterative manner to determine the required TRN

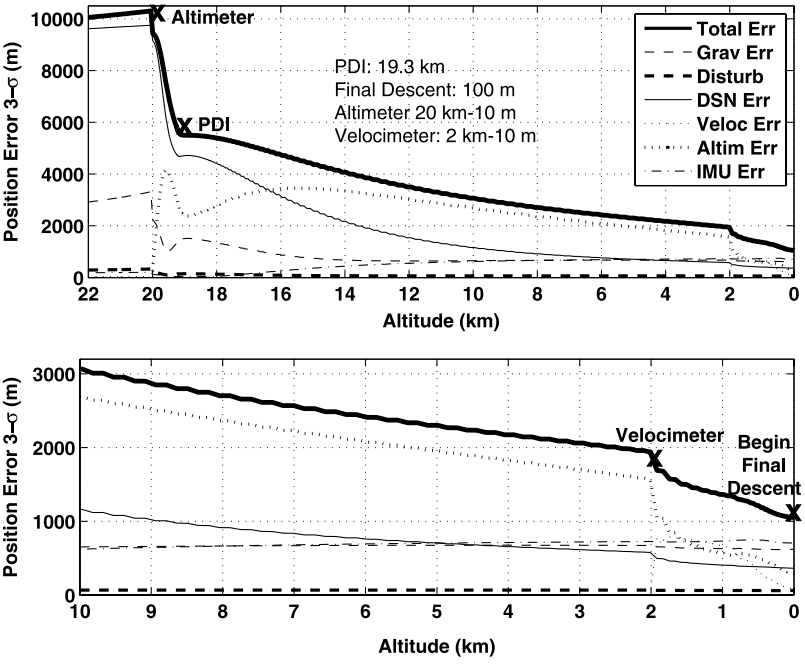

Fig. 5 Total inertial navigation position uncertainty and individual components (low trajectory).

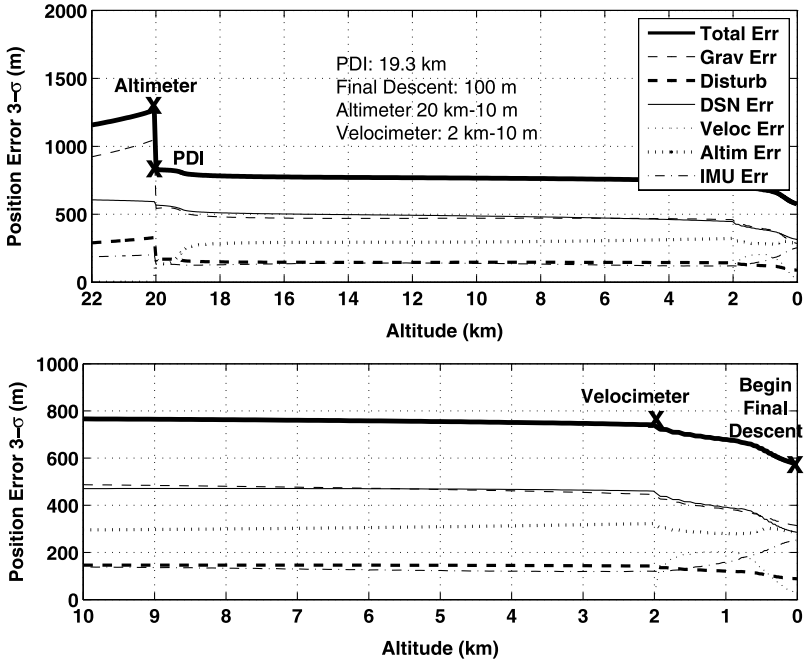

Fig. 6 Total inertial navigation position uncertainty and individual components with gravity model error compensation and low initial state uncertainties (low trajectory).

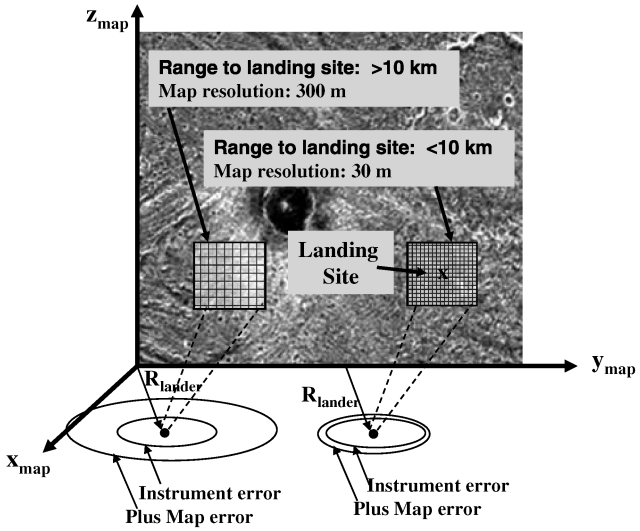

Fig. 7 TRN error model showing instrument error and map error.

instrument accuracy (positional or angular) needed to meet a 100 m 3-σ landing knowledge requirement.

B. Terrain-Relative Navigation Operating Range

Initially it may seem reasonable to assume that the TRN system will operate through a large portion of the lunar descent trajectory (e.g., from PDI through landing). But *requiring* the TRN system to operate over a wide range of altitudes, velocities, and rotation rates may not be practical. In addition, if we require terrain maps to cover thousands of square kilometers from PDI though landing, it may not be practical from either a TRN instrument perspective (e.g., onboard memory requirements) or from a mapping mission perspective. Thus, with simplicity as a goal, the analysis that follows examines the effects of operating the TRN for only a brief period of time. Five different operating regions were selected for both the high and low trajectories. as shown in Table 8 and Fig. 8. The duration of each operating region is 60 s. Region I is near the end of the descent trajectory, and each subsequent region occurs 60 s earlier with the exception of region V, which is 60 s before PDI. In each of these regions, three different TRN measurement sample rates are investigated: 1) a single measurement taken at the beginning of the operating region, 2) measurements every 30 s, and 3) measurements every 10 s.

C. Analysis Results, Sensitivities, and Major Findings

LinCov tools are typically used to determine overall navigation performance as a function of time. For the inertial navigation analysis in Sec. V, we also conducted a sensitivity analysis [11] to determine the contribution of each source of uncertainty to the overall navigation budget. This was accomplished by running the LinCov tool one time for each source of error while turning off all the other sources of error. For this TRN analysis, we tried something new. After completing the sensitivity analysis, we used linear extrapolation to estimate and compute the level of TRN sensor error that would produce a total position error (due to all sources of error) equal

Table 7 TRN measurement error model parameters

Type	Error model parameters (1-σ)	Comments
Position TRN	*Measurement bias*	Attitude uncertainty and terrain map resolution produce additional error
	Altitude, downrange, cross track $\sigma_{\text{pos}}/5$, σ_{pos}, σ_{pos} ($\tau = 100$ s)	
	Measurement noise	
	Altitude, downrange, cross track $\sigma_{\text{pos}}/5$, σ_{pos}, σ_{pos}	
	Misalignment, scale factor	
	50 arcsecond, 0.01% ($\tau = 100$ s)	
Angles TRN	*Angle bias*	Attitude uncertainty and terrain map resolution produce additional error
	σ_{ang} ($\tau = 100$ s)	
	Angle noise	
	σ_{ang}	

Table 8 TRN operating regions

	TRN operating regions (high trajectory)				
	I	II	III	IV	V (Pre-PDI)
Altitude	0.5–2 km	2–4 km	48 km	8–12 km	17.0–17.3 km
Range	0 km	0–0.6 km	0.6–15 km	15–48 km	300–370 km
Duration	60 s	60 s	60 s	60 s	60 s
	TRN operating regions (low trajectory)				
	I	II	III	IV	V (Pre-PDI)
Altitude	0.2–2.5 km	2.5–8 km	8–14 km	14–17.5 km	19.2–19.5 km
Range	0–4.8 km	4.8–28.5 km	28.5–75 km	75 km–135 km	315–382 km
Duration	60 s	60 s	60 s	60 s	60 s

to 100 m 3-σ. With this estimate, we reran the sensitivity analysis and recomputed the total position error. The process was repeated until we found the level of TRN sensor error that resulted in precisely a 100 m 3-σ total position. This is a novel technique that requires only one or two iterations to converge. This entire process is then repeated for different measurement sample rates, TRN operating regions, TRN measurement types (positional or angular), and reference trajectories (high or low).

The results are given in Figs. 9–12. These figures show the required TRN instrument accuracy (positional or angular) to meet the 100 m 3-σ knowledge error at landing as a function of the measurement sample rate and the TRN operating region. Shaded cells indicate that the 100 m 3-σ knowledge error could not be met. Even with a perfect TRN instrument, the cumulative effect of gyro, accelerometer, and star-camera errors after the TRN operating period resulted in landing knowledge errors greater than 100 m 3-σ. The final landing errors using perfect TRN sensors are indicated in the shaded cells. Unshaded cells show where the operation of the TRN can achieve a 100 m 3-σ landing *knowledge* error. The required TRN sensor specifications are indicated in these cells. It is important to point out that, even though a TRN sensor operating in region I can meet the 3-σ landing *knowledge* requirement, in region I it may be too late in the trajectory to correct for trajectory dispersions and meet the 3-σ total landing-error requirement. This is true for all region I analysis, high and low trajectories, and positional and angular TRN measurements. Selected time histories of relative navigation errors and the sensitivities of the relative navigation errors to map error, baseline inertial instrument error, and TRN error are given in Figs. A1–A10 in Appendix A. The following are the major findings from the TRN analysis results and analysis sensitivities.

There is a 60–120 s period from regions II to III of the high trajectory and a 60 s period in region II of the low trajectory (indicated by unshaded cells in those regions) where TRN is available early enough in the trajectory to provide dispersion control and late enough to achieve the 100 m 3-σ landing knowledge error without being overburdened with operating range requirements, terrain mapping requirements, and TRN instrument requirements. This conclusion is a strong function of when high-resolution terrain maps become available along the descent trajectory. It is also a strong function of when it becomes too late to recover from trajectory dispersions. These conclusions need to be verified by focusing specifically on this special operating region. Sensitivities to terrain map resolution and dispersion control capabilities also need to be determined.

There is a 60 s period near the end of the high trajectory (region II) in which a single TRN measurement may provide sufficient relative position/velocity knowledge early enough in the trajectory to provide dispersion control and late enough to meet the 100 m 3-σ landing error. This conclusion needs to be verified by focusing specifically on this special operating region.

The regions in which TRN cannot meet the 100 m 3-σ knowledge error at landing (shaded cells) are the regions in which the map resolution is poor (300 m 3-σ) and occur at TRN operating ranges greater than 10 km. The regions in which TRN can meet the 100 m 3-σ knowledge error at landing (unshaded cells) are the regions in which the map resolution is high (30 m 3-σ) and occur at operating ranges less than 10 km.

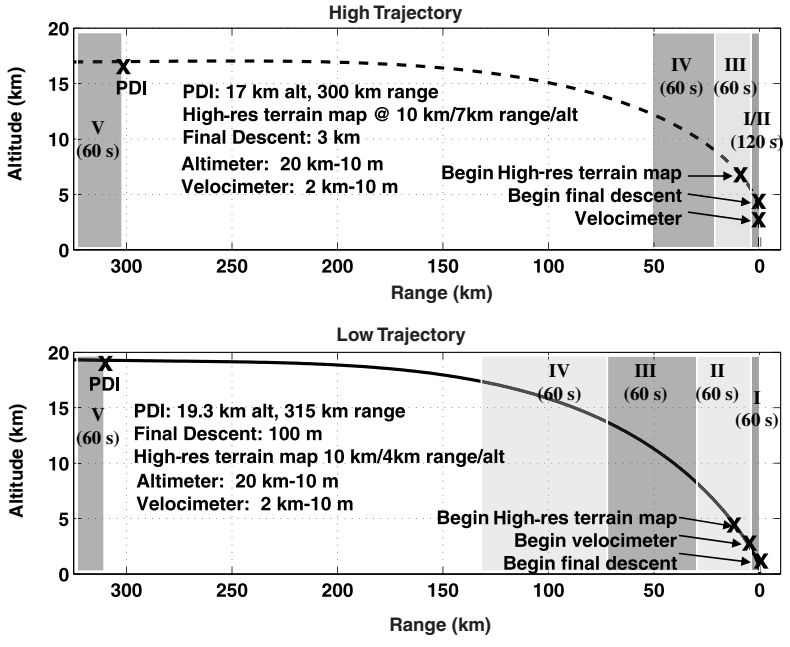

Fig. 8 TRN operating regions.

Required TRN Sensor Performance Using Position Measurements (high trajectory)

		Operating Range (altitude) I	II	III	IV	V
		0.5 -2 km (60 s)	2 – 4 km (60 s)	4 – 8 km (60 s)	8-12 km (60 s)	Pre-PDI 17-17.3 km (60 s)
Sample Rate	Once (1 meas)	41 m	33 m	Can not meet requirement 400m at landing	Can not meet requirement 405 m at landing	Can not meet requirement 515 m at landing
	Every 30 s (2 meas)	52 m	70 m	26 m	Can not meet requirement 305 m at landing	Can not meet requirement 440 m at landing
	Every 10 s (6 meas)	60 m	117 m	43 m	Can not meet requirement 200 m at landing	Can not meet requirement 380 m at landing

Vel (< 2 km) | 7 km alt, 10 km range
High-resolution terrain map | Low-resolution terrain map

Fig. 9 Required TRN sensor performance using relative position measurements to meet the 100 m 3-σ landing knowledge error requirement (high trajectory).

Required TRN Sensor Performance Using Angular Measurements (high trajectory)

		Operating Range (altitude) I	II	III	IV	V
		0.5 -2 km (60 s)	2 – 4 km (60 s)	4 – 8 km (60 s)	8-12 km (60 s)	Pre-PDI 17-17.3 km (60 s)
Sample Rate	Once (1 meas)	0.03 rad	0.009 rad	Can not meet requirement 377m at landing	Can not meet requirement 400 m at landing	Can not meet requirement 505 m at landing
	Every 30 s (2 meas)	0.06 rad	0.02 rad	0.003 rad	Can not meet requirement 295 m at landing	Can not meet requirement 435 m at landing
	Every 10 s (6 meas)	0.10 rad	0.03 rad	0.009 rad	Can not meet requirement 190 m at landing	Can not meet requirement 380 m at landing

Vel (< 2 km) | 7 km alt, 10 km range
High-resolution terrain map | Low-resolution terrain map

Fig. 10 Required TRN sensor performance using angle measurements to meet the 100 m 3-σ landing knowledge error requirement (high trajectory).

Required TRN Sensor Performance Using Position Measurements (low trajectory)

		Operating Range (altitude) I	II	III	IV	V
		0.2 -2.5 km (60 s)	2.5 – 8 km (60 s)	8 - 14 km (60 s)	14 -17.5 km (60 s)	Pre-PDI 19.2 – 19.5 km (60 s)
Sample Rate	Once (1 meas)	41 m	Can not meet requirement 400m at landing	Can not meet requirement 400m at landing	Can not meet requirement 405 m at landing	Can not meet requirement 430 m at landing
	Every 30 s (2 meas)	54 m	Can not meet requirement 295m at landing	Can not meet requirement 300m at landing	Can not meet requirement 305 m at landing	Can not meet requirement 330 m at landing
	Every 10 s (6 meas)	94 m	42 m	Can not meet requirement 175m at landing	Can not meet requirement 200 m at landing	Can not meet requirement 240 m at landing

Vel (< 2 km) | 4 km alt, 10 km range
High-res terrain map | Low-resolution terrain map

Fig. 11 Required TRN sensor performance using relative position measurements to meet the 100 m 3-σ landing knowledge error requirement (low trajectory).

Required TRN Sensor Performance Using Angular Measurements (low trajectory)

		Operating Range (altitude) I	II	III	IV	V
		0.2 -2.5 km (60 s)	2.5 – 8 km (60 s)	8 - 14 km (60 s)	14 -17.5 km (60 s)	Pre-PDI 19.2 – 19.5 km (60 s)
Sample Rate	Once (1 meas)	0.02 rad	Can not meet requirement 390m at landing	Can not meet requirement 400m at landing	Can not meet requirement 405 m at landing	Can not meet requirement 410 m at landing
	Every 30 s (2 meas)	0.06 rad	Can not meet requirement 285m at landing	Can not meet requirement 295m at landing	Can not meet requirement 300 m at landing	Can not meet requirement 320 m at landing
	Every 10 s (6 meas)	0.34 rad	0.015 rad	Can not meet requirement 170m at landing	Can not meet requirement 200 m at landing	Can not meet requirement 235 m at landing

Vel (< 2 km) | 4 km alt, 10 km range
High-res terrain map | Low-resolution terrain map

Fig. 12 Required TRN sensor performance using angle measurements to meet the 100 m 3-σ landing knowledge error requirement (low trajectory).

As a general rule, in regions in which TRN can meet the 100 m 3-σ knowledge error at landing (unshaded cells), the TRN instrument accuracy requirements are higher with increasing altitude/range from the landing site and lower with increasing sample rate. The exception to this rule occurs when comparing regions I and II of the high trajectory and is due to a strong coupling between TRN and velocimeter measurements.

Additionally, the sensitivity data in Appendix A clearly indicate the following trends: 1) poor-resolution terrain map errors (300 m 3-σ) dominate the relative navigation error before the lander encounters terrain with high-resolution maps; 2) with high-resolution terrain maps (30 m 3-σ), the relative navigation error is dominated by TRN instrument error with the exception of high-trajectory region III data, for which the baseline inertial instrument errors begin to compete with the TRN errors; and 3) in all cases, map-tie error, or the uncertainty of the inertial location of the landing site, does not have a significant impact on the total relative navigation error.

VII. Conclusions

In this paper, a 165-state LinCov tool was used to conduct a detailed analysis of the powered lunar descent and landing navigation problem. Although hundreds of runs were required to compute the inertial and relative navigation errors and their sensitivities to environment, sensor, and initial state errors, the total required CPU time was minimal given that each run required less than 30 s of CPU time on a common laptop computer.

The LinCov analysis showed that the 1 km 3-σ final landing uncertainties for the baseline trajectories are reduced to 500–600 m 3-σ when using *low* initial state errors and gravity error compensation. Although this is good performance, it is not sufficient to meet the 100 m 3-σ relative position knowledge requirement and justifies some form of terrain- or landing-site-relative navigation.

The altimeter plays a significant role in reducing navigation knowledge error before PDI and during the braking maneuver. Sufficient time should be allowed before PDI to extract as much information from the altimeter data as possible. This may require a small increase in the operating altitude of the altimeter from 20 to 25 km, but the benefit will be a more accurate navigation state at PDI without requiring a high-altitude surface feature tracking system.

There is a 1–2 min period near the end of both the high and low trajectories during which TRN is available early enough in the trajectory to provide dispersion control and late enough to achieve the 100 m 3-σ landing error without being overburdened with operating range requirements, terrain mapping requirements, and TRN instrument requirements. This conclusion is a strong function of when high-resolution terrain maps become available along the descent trajectory. It is also a strong function of when it becomes too late to recover from trajectory dispersions. These conclusions need to be verified by focusing specifically on this special operating region. Sensitivities to terrain map resolution and dispersion control capabilities need to be determined.

Finally, there is a 60 s period near the end of the high trajectory (region II) during which a *single* TRN measurement may provide sufficient relative position/velocity knowledge early enough in the trajectory to provide dispersion control and late enough to meet the 100 m 3-σ landing error. Future analysis should also be focused on this special operating region.

Appendix A: Terrain-Relative Navigation Error Time Histories and Sensitivities

The figures below correspond to the unshaded cells in Figs. 9–12 with 10 s TRN measurement rates. Each figure shows the total relative navigation error and the contribution of each error source to the total error. The component error sources are terrain map error, map-tie error (the uncertainty of the inertial location of the landing site), baseline inertial instrument error, and TRN instrument error. The rss of the individual component contributions equals the total navigation error, and each contribution is proportional to the error

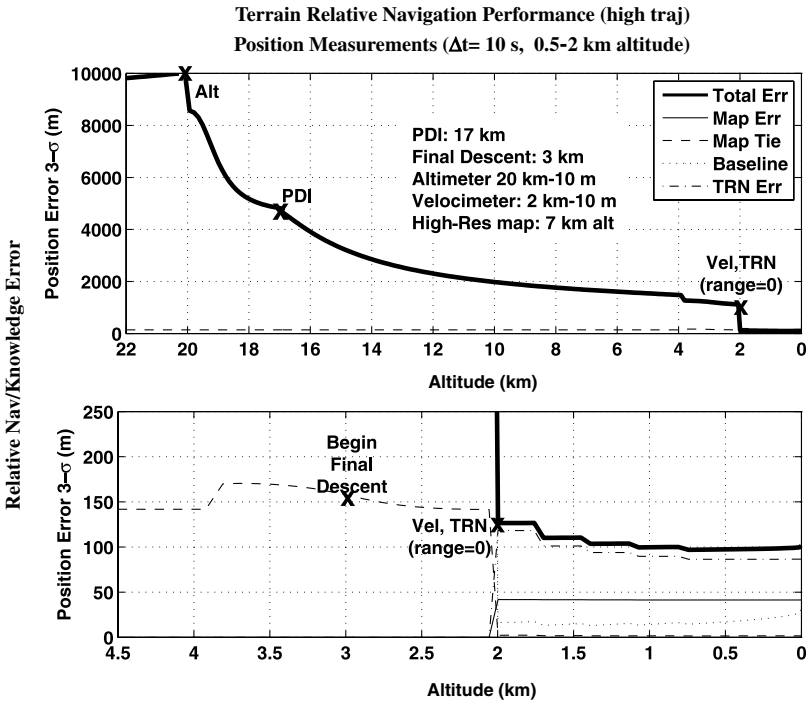

Fig. A1 Total TRN relative position uncertainty and individual components using position measurements (high trajectory).

source. If terrain map errors or TRN instrument errors are doubled, their contributions to the total navigation error will double. If their errors are halved, their contributions to the total will be halved. If a particular component error is a large fraction of the total error, doubling or halving the error source will double or halve the total. Thus, these charts can be used by system designers to determine when a better sensor, subsystem, or terrain map may provide significant improvement in the overall system or when a less expensive, less accurate sensor, subsystem, or terrain map may suffice without compromising the overall performance of the system.

Appendix B: Matrix Partial Derivatives

The propagation of the navigation state $\dot{\hat{x}} = \hat{f}(\hat{x}, \hat{u}, \tilde{y})$ is accomplished using Eqs. (46–51). The propagation of the navigation state covariance matrix in Eq. (55) is accomplished using the following partial derivative and state process noise covariances (for the order of the states, see Fig. 1). Note that, for the linear covariance analysis, the partial derivatives here have been evaluated along the nominal state vector. This includes the nominal lander position, velocity, attitude, and angular velocity and the nominal landing-site position. All other states including biases, scale factors, and misalignments are nominally zero.

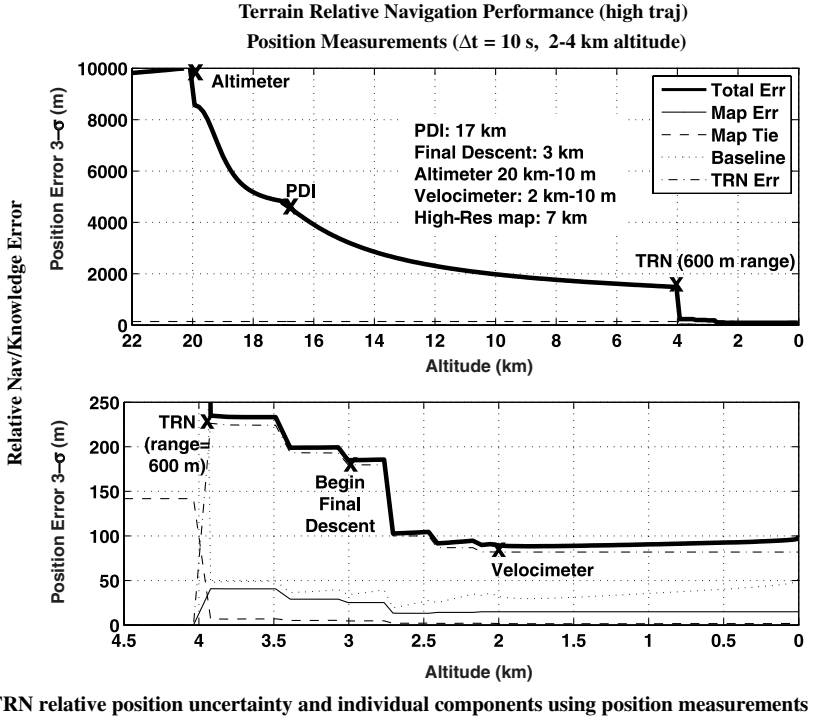

Fig. A2 Total TRN relative position uncertainty and individual components using position measurements (high trajectory).

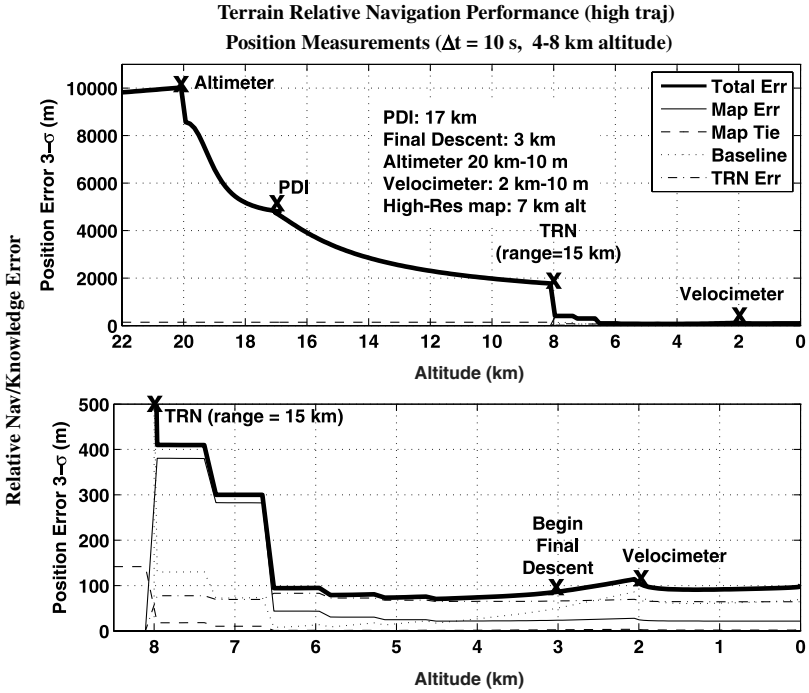

Fig. A3 Total TRN relative position uncertainty and individual components using position measurements (high trajectory).

$$\hat{F}_{\hat{x}} = \frac{\partial \hat{\boldsymbol{f}}}{\partial \hat{\boldsymbol{x}}} = \begin{pmatrix} \hat{D}_{\hat{a}} & \hat{D}_{\hat{p}} & \hat{D}_{\hat{e}} \\ 0_{63\times 12} & -\mathrm{Diag}([\frac{1}{\hat{\tau}_1}, \frac{1}{\hat{\tau}_2}, \ldots, \frac{1}{\hat{\tau}_{63}}]) & 0_{63\times 6} \\ 0_{6\times 12} & 0_{6\times 63} & -\mathrm{Diag}([\frac{|\hat{v}^i|}{\hat{d}_1}, \frac{|\hat{v}^i|}{\hat{d}_2}, \ldots, \frac{|\hat{v}^i|}{\hat{d}_6}]) \end{pmatrix} \tag{B1}$$

$$\hat{S}_{\eta} = \begin{pmatrix} \hat{S}_{\eta_d} & 0_{12\times 63} & 0_{12\times 6} \\ 0_{63\times 12} & 0_{63\times 63} & 0_{63\times 6} \\ 0_{6\times 12} & 0_{6\times 63} & 0_{6\times 6} \end{pmatrix} \tag{B2}$$

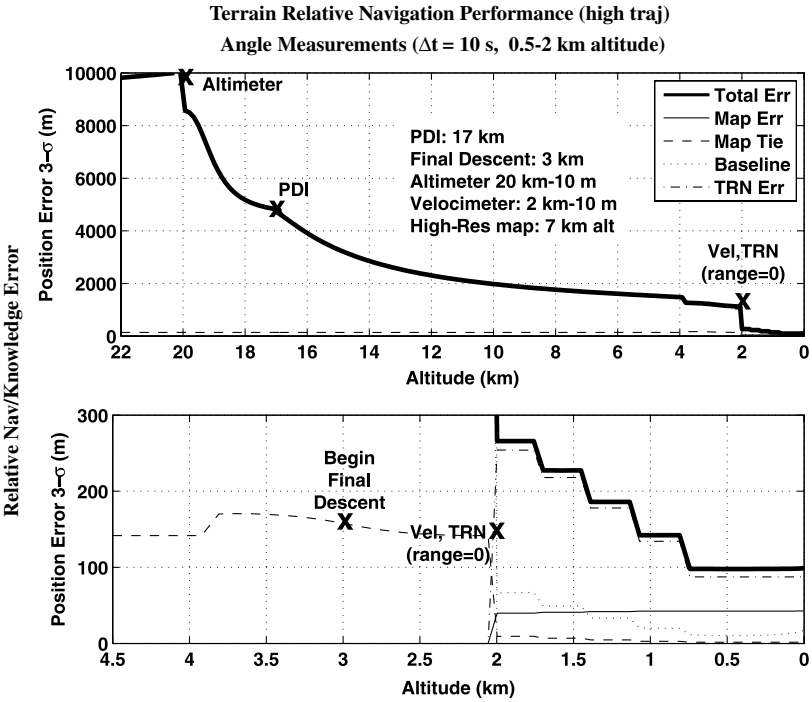

Fig. A4 Total TRN relative position uncertainty and individual components using angle measurements (high trajectory).

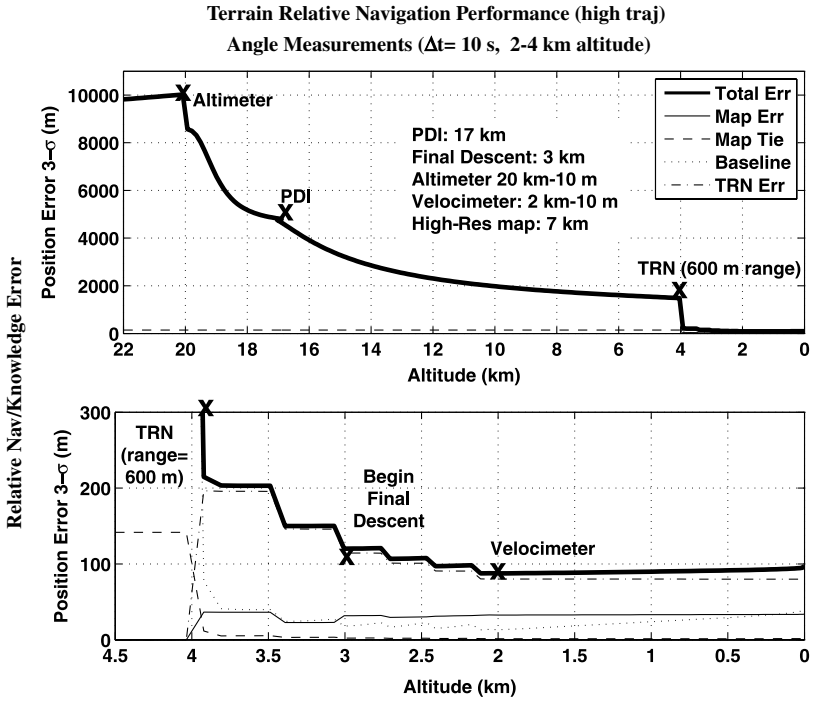

Fig. A5 Total TRN relative position uncertainty and individual components using angle measurements (high trajectory).

$$\hat{S}_w = \begin{pmatrix} \hat{S}_{a_d} & 0_{12\times 63} & 0_{12\times 6} \\ 0_{63\times 12} & -\mathrm{Diag}([\hat{\sigma}^2_{p_1}, \hat{\sigma}^2_{p_2}, \ldots, \hat{\sigma}^2_{p_{63}}]) & 0_{63\times 6} \\ 0_{6\times 12} & 0_{6\times 63} & -\mathrm{Diag}([\hat{\sigma}^2_{\varepsilon_1}, \hat{\sigma}^2_{\varepsilon_2}, \ldots, \hat{\sigma}^2_{\varepsilon_6}]) \end{pmatrix} \tag{B3}$$

where

$$\hat{D}_{\hat{d}} = \begin{pmatrix} [\boldsymbol{\omega}^i_{\mathrm{moon}}\times] & 0_{3\times 3} & 0_{3\times 3} & 0_{3\times 3} \\ 0_{3\times 3} & 0_{3\times 3} & I_{3\times 3} & 0_{3\times 3} \\ 0_{3\times 3} & \frac{\partial \hat{\boldsymbol{a}}^l_{\mathrm{grav}}}{\partial \hat{\boldsymbol{r}}^l} & 0_{3\times 3} & -\hat{\mathcal{T}}^i_\ell[\tilde{\boldsymbol{a}}^l_{\mathrm{accel}}\times] \\ 0_{3\times 3} & 0_{3\times 3} & 0_{3\times 3} & -[\tilde{\boldsymbol{\omega}}^\ell\times] \end{pmatrix} \tag{B4}$$

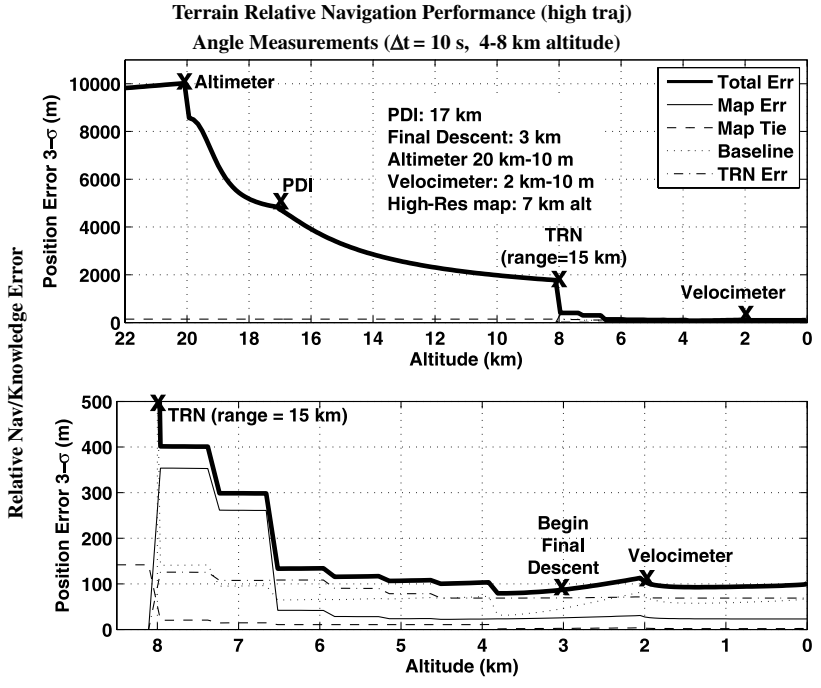

Fig. A6 Total TRN relative position uncertainty and individual components using angle measurements (high trajectory).

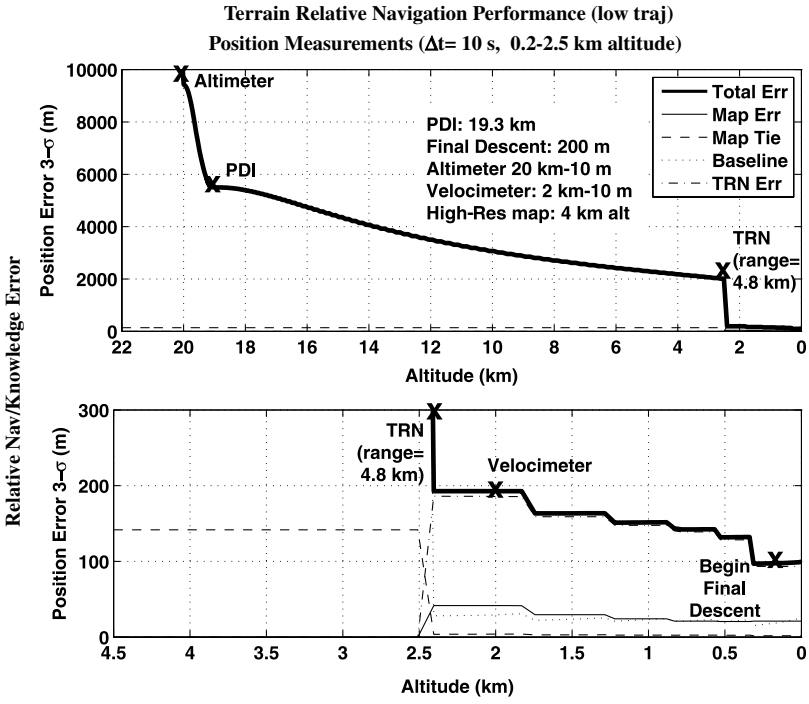

Fig. A7 Total TRN relative position uncertainty and individual components using position measurements (low trajectory).

$$\hat{D}_{\hat{p}} = \begin{pmatrix} 0_{3\times18} & 0_{3\times3} & 0_{3\times3} & 0_{3\times3} & 0_{3\times3} & 0_{3\times3} & 0_{3\times3} & 0_{3\times27} \\ 0_{3\times18} & 0_{3\times3} & 0_{3\times3} & 0_{3\times3} & 0_{3\times3} & 0_{3\times3} & 0_{3\times3} & 0_{3\times27} \\ 0_{3\times18} & \hat{T}^i_\ell \mathrm{Diag}(\tilde{\boldsymbol{a}}^\ell_{\mathrm{accel}}) & \hat{T}^i_\ell [\tilde{\boldsymbol{a}}^\ell_{\mathrm{accel}}\times] & I_{3\times3} & 0_{3\times3} & 0_{3\times3} & 0_{3\times3} & 0_{3\times27} \\ 0_{3\times18} & 0_{3\times3} & 0_{3\times3} & 0_{3\times3} & \mathrm{Diag}(\tilde{\boldsymbol{\omega}}^\ell) & [\tilde{\boldsymbol{\omega}}^\ell\times] & I_{3\times3} & 0_{3\times27} \end{pmatrix} \tag{B5}$$

$$\hat{D}_{\hat{e}} = \begin{pmatrix} 0_{3\times3} & 0_{3\times3} \\ 0_{3\times3} & 0_{3\times3} \\ 0_{3\times3} & I_{3\times3} \\ 0_{3\times3} & 0_{3\times3} \end{pmatrix} \tag{B6}$$

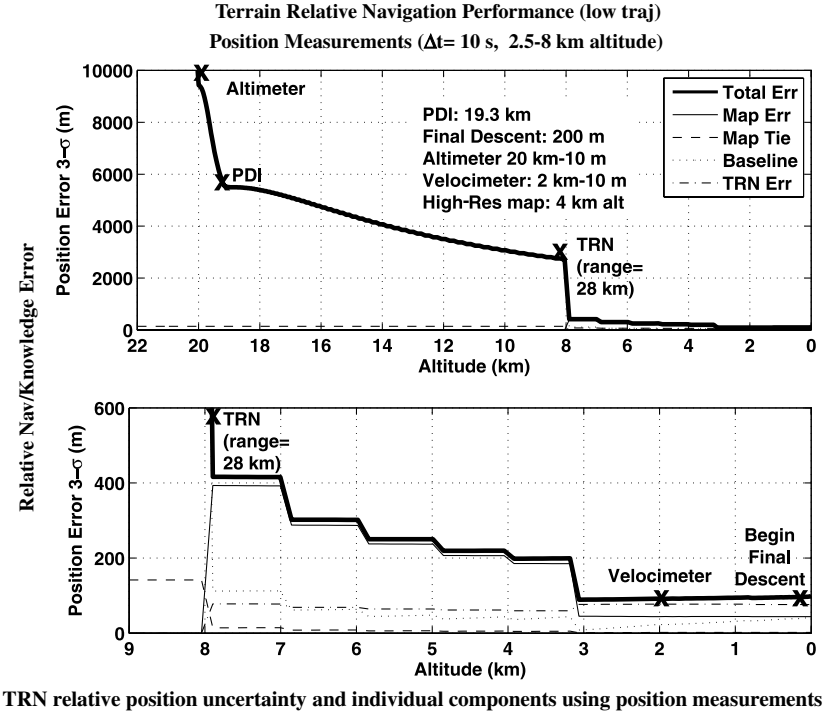

Fig. A8 Total TRN relative position uncertainty and individual components using position measurements (low trajectory).

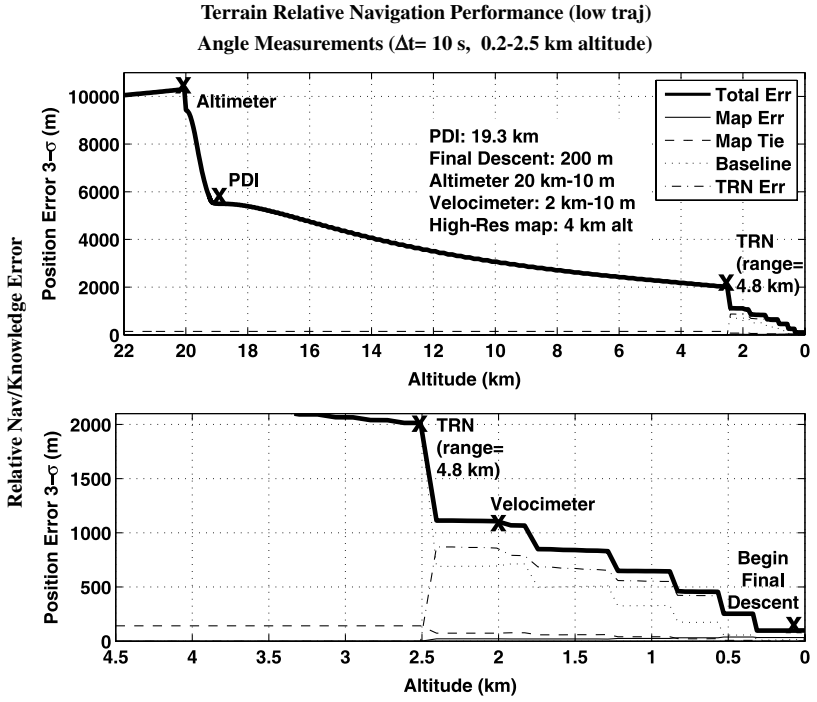

Fig. A9 Total TRN relative position uncertainty and individual components using angle measurements (low trajectory).

$$\hat{S}_{\eta_d} = \begin{pmatrix} 0_{3\times3} & 0_{3\times3} & 0_{3\times3} & 0_{3\times3} \\ 0_{3\times3} & 0_{3\times3} & 0_{3\times3} & 0_{3\times3} \\ 0_{3\times3} & 0_{3\times3} & \hat{S}_{\eta_{\text{accel}}} & 0_{3\times3} \\ 0_{3\times3} & 0_{3\times3} & 0_{3\times3} & \hat{S}_{\eta_{\text{gyro}}} \end{pmatrix}$$

$$\hat{S}_{a_d} = \begin{pmatrix} 0_{3\times3} & 0_{3\times3} & 0_{3\times3} & 0_{3\times3} \\ 0_{3\times3} & 0_{3\times3} & 0_{3\times3} & 0_{3\times3} \\ 0_{3\times3} & 0_{3\times3} & \hat{S}_a & 0_{3\times3} \\ 0_{3\times3} & 0_{3\times3} & 0_{3\times3} & 0_{3\times3} \end{pmatrix} \tag{B7}$$

The measurement sensitivity matrix for the velocimeter is given by

$$\hat{H}^{\text{vel}}_{\hat{x}} = (0_{3\times3}, -\hat{T}^{\text{vel}}_i[\boldsymbol{\omega}^i_{\text{moon}}\times], \hat{T}^{\text{vel}}_i, [\hat{\mathbf{v}}^{\text{vel}}_{\text{rel}}\times]\hat{T}^{\text{vel}}_\ell, 0_{3\times18}, \text{Diag}(\hat{\mathbf{v}}^{\text{vel}}_{\text{rel}}), [\hat{\mathbf{v}}^{\text{vel}}_{\text{rel}}\times], I_{3\times3}, 0_{3\times36}, 0_{3\times6}) \tag{B8}$$

The flight computer's value of the velocimeter measurement covariance is given by

$$\hat{R}^{\text{vel}}_{\nu} = \text{Diag}([\hat{\sigma}^2_{\text{vel}_x}, \hat{\sigma}^2_{\text{vel}_y}, \hat{\sigma}^2_{\text{vel}_z}]) \tag{B9}$$

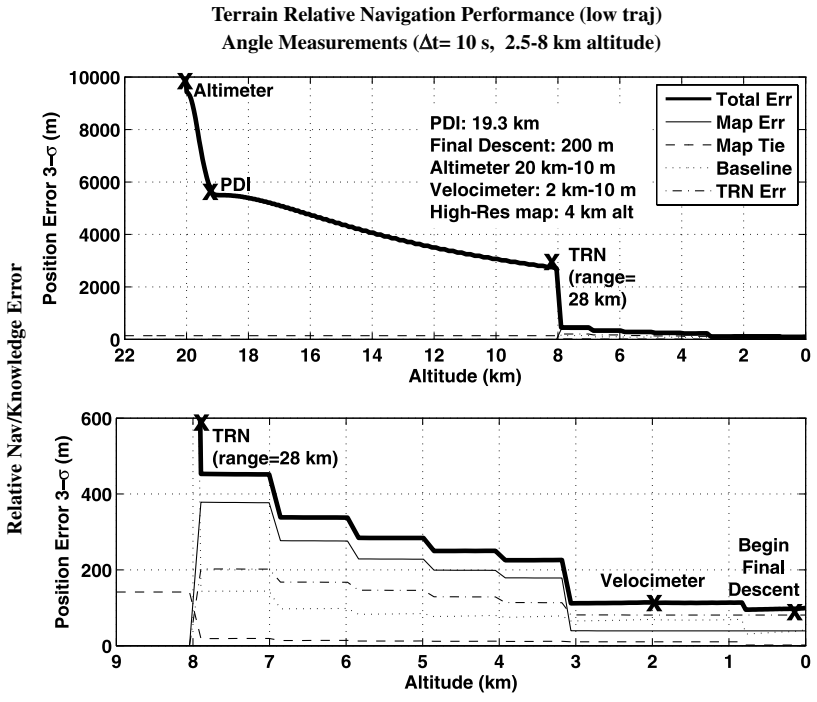

Fig. A10 Total TRN relative position uncertainty and individual components using angle measurements (low trajectory).

The measurement sensitivity matrix for the TRN position sensor is given by

$$\hat{H}_{\hat{x}}^{\text{trnpos}} = (\hat{\mathcal{T}}_i^{\text{trn}}, -\hat{\mathcal{T}}_i^{\text{trn}}, 0_{3\times3}, [\hat{\mathbf{r}}_{\Delta r}^{\text{trn}}\times]\hat{\mathcal{T}}_\ell^{\text{trn}}, 0_{3\times27}, \text{Diag}(\hat{\mathbf{r}}_{\Delta r}^{\text{trn}}), [\hat{\mathbf{r}}_{\Delta r}^{\text{trn}}\times], I_{3\times3}, 0_{3\times27}, \hat{\mathcal{T}}_s^{\text{trn}}, 0_{3\times3}) \tag{B10}$$

The flight computer's value of the TRN position sensor measurement covariance is given by

$$\hat{R}_v^{\text{trnpos}} = \text{Diag}([\hat{\sigma}^2_{\text{trnpos}_x}, \hat{\sigma}^2_{\text{trnpos}_y}, \hat{\sigma}^2_{\text{trnpos}_z}]) \tag{B11}$$

The measurement sensitivity matrix for the TRN angle sensor is given by

$$\hat{H}_{\hat{x}}^{\text{trnang}} = \begin{pmatrix} 1/\hat{l}_z & 0 & -\hat{l}_x/\hat{l}_z^2 \\ 0 & 1/\hat{l}_z & -\hat{l}_y/\hat{l}_z^2 \end{pmatrix} \frac{\partial \hat{\boldsymbol{l}}_{\text{los}}^{\text{trn}}}{\partial \hat{\mathbf{x}}} \tag{B12}$$

where

$$\frac{\partial \hat{\boldsymbol{l}}_{\text{los}}^{\text{trn}}}{\partial \hat{\mathbf{x}}} = (\hat{\mathcal{T}}_i^{\text{trn}}, -\hat{\mathcal{T}}_i^{\text{trn}}, 0_{3\times3}, [\hat{l}_{\text{los}}^{\text{trn}}\times]\hat{\mathcal{T}}_\ell^{\text{trn}}, 0_{3\times60}, [\hat{l}_{\text{los}}^{\text{trn}}\times], \hat{\mathcal{T}}_s^{\text{trn}}, 0_{3\times3}) \tag{B13}$$

The flight computer's value of the TRN angle sensor measurement covariance is given by

$$\hat{R}_v^{\text{trnang}} = \text{Diag}([\hat{\sigma}^2_{\text{trnang}_x}, \hat{\sigma}^2_{\text{trnang}_y}]) \tag{B14}$$

The measurement sensitivity matrix for the star camera is given by

$$\hat{H}_{\hat{x}}^{\text{starcam}} = (\,0_{3\times9} \quad \hat{\mathcal{T}}_\ell^{\text{starcam}} \quad 0_{3\times57} \quad I_{3\times3} \quad 0_{3\times9}\,) \tag{B15}$$

The flight computer's value of the star-camera measurement covariance is given by

$$\hat{R}_v^{\text{starcam}} = \text{Diag}([\hat{\sigma}^2_{\text{starcam}_x}, \hat{\sigma}^2_{\text{starcam}_y}, \hat{\sigma}^2_{\text{starcam}_z}]) \tag{B16}$$

The measurement sensitivity matrix for the altimeter is given by

$$\hat{H}_{\hat{x}}^{\text{alt}} = (\,0_{1\times3} \quad (\hat{\mathbf{r}}^i)^T/|\hat{\mathbf{r}}^i| \quad 0_{1\times6} \quad 0_{1\times60} \quad (|\hat{\mathbf{r}}^i| - \rho_{\text{moon}}) \quad 1 \quad 1 \quad 0_{1\times6}\,) \tag{B17}$$

The flight computer's value of the altimeter's measurement covariance is simply given by

$$\hat{R}_v^{\text{alt}} = \hat{\sigma}^2_{v_{\text{alt}}} \tag{B18}$$

References

[1] Geller, D. K., "Linear Covariance Techniques for Orbital Rendezvous Analysis and Autonomous Onboard Mission Planning," *Journal of Guidance, Control, and Dynamics*, Vol. 29, No. 6, 2006, pp. 1404–1414. doi:10.2514/1.19447

[2] Woffinden, D. C., and Geller, D. K., "Relative Angles-Only Navigation and Pose Estimation for Autonomous Orbital Rendezvous," *Journal of Guidance, Control, and Dynamics*, Vol. 30, No. 5, Sept.–Oct. 2007, pp. 1455–1469. doi:10.2514/1.28216

[3] Barton, G. H., Shepperd, S. W., and Brand, T. J., "Autonomous Lunar Landing Navigation," American Astronautical Society Paper 94-120, Aug. 1994.

[4] DeMars, K. J., and Bishop, R. H., "Precision Descent Navigation for Landing at the Moon," American Astronautical Society Paper 07-314, Aug. 2007.

[5] Davis, J. L., and Striepe, S. A., "Advances in POST2 End-to-End Descent and Landing Simulation for the ALHAT Project," AIAA Paper 2008-6938, Aug. 2008.

[6] Wollenhaupt, W. R., "Apollo Orbit Determination and Navigation," AIAA Paper 70-27, Jan. 1970.

[7] Geller, D. K., "Analysis of the Relative Attitude Estimation and Control Problem for Satellite Inspection and Orbital Rendezvous," *Journal of the Astronautical Sciences*, Vol. 55, No. 2, April–June 2007, pp. 195–214.

[8] Kaplan, M. H., *Modern Spacecraft Dynamics and Control*, Wiley, New York, 1976, pp. 343–370.

[9] Pittelkau, M. E., "Rotation Vector in Attitude Estimation," *Journal of Guidance, Control, and Dynamics*, Vol. 26, No. 6, 2003, pp. 855–860. doi:10.2514/2.6929

[10] Lefferts, E. J., Markley, F. L., and Shuster, M. D., "Kalman Filtering for Spacecraft Estimation," *Journal of Guidance, Control, and Dynamics*, Vol. 5, No. 5, 1982, pp. 417–429. doi:10.2514/3.56190

[11] Maybeck, P. S., *Stochastic Models, Estimation, and Control*, Academic Press, New York, 1979.

[12] Epp, C. D., and Smith, T. B., "Autonomous Precision Landing and Hazard Detection and Avoidance Technology (ALHAT)," Institute of Electrical and Electronics Engineers Paper AC 1379, March 2007.

[13] Brady, T., Schwartz, J., and Tillier, C., "System Architecture and Operational Concept for an Autonomous Precision Lunar Landing System," American Astronautical Society Paper 07-053, Feb. 2007.

[14] Roberson, W., "Lunar Gravity Disturbance Models: Point-Mass and Statistical," Draper Lab., GCB 05-075, 2006.

[15] D'Souza, C., "Process Noise for Lunar Missions," NASA Johnson Space Center EG-CX-06-03, 2006.

B. Marchand
Associate Editor